

ABSTRACT

Title of Thesis: PRESSURELESS SINTERING OF POWDER PROCESSED
FUNCTIONALLY GRADED METAL-CERAMIC PLATES

Michael Louis Pines, Master of Science, 2004

Thesis Directed by: Associate Professor Hugh Bruck
Department of Mechanical Engineering

The need exists to fabricate graded metal-ceramic composite armor specimens consisting of nickel and alumina through powder processing techniques and pressureless sintering for dynamic mechanical characterization. An approach is employed to control the thermal shrinkage of each microstructure during sintering by varying particle sizes of the two powders. Models were developed to understand both the nature of the porosity during sintering and the shrinkage behaviors of the composites. The relationship between porosity and sintered properties was characterized through microhardness measurements, indicating the reinforcing particles are debonded from the matrix and can be treated as additional porosity. The type of microstructure to be used in property models was characterized through optical microscopy. Porosity effects were incorporated into constitutive equations for a recently developed finite element sintering model, which was validated through comparison of predicted and experimental shape profiles of graded specimens and through correlation of stress profiles to fracture locations.

PRESSURELESS SINTERING OF POWDER PROCESSED FUNCTIONALLY
GRADED METAL-CERAMIC PLATES

by

Michael Louis Pines

Thesis submitted to the Faculty of the Graduate School of the
University of Maryland, College Park in partial fulfillment
of the requirements for the degree of
Master of Science
2004

Advisory Committee

Associate Professor Hugh Bruck, Chair/Advisor
Professor Abhijit Dasgupta
Associate Professor F. Patrick McCluskey

©Copyright by

Michael Louis Pines

2004

Acknowledgement

I would like to thank all of those people who helped me complete the requirements for my graduate degree. Without the support of these people, I would have been unable to complete this work.

I would first like to thank my advisor, Associate Professor Hugh Bruck, for all of the support he has given me, and all of the knowledge he has shared with me. He kept me focused and taught me to trust in my own abilities.

I would also like to thank the members of my committee, Professor Abhijit Dasgupta and Associate Professor Patrick McCluskey, for taking the time out of their schedules to take part in my thesis defense.

I would like to thank my colleague, Dr. Yasser Mohamed Shabana, whose input and hard work was invaluable towards my completion of this work. He was always willing to make time for me, and I am very appreciative for that.

I would finally like to thank my lab mates, who are too numerous to list, for adding important input whenever it was needed (and sometimes when it was not) and for supporting me as I worked to finish up my work, and all of my family and friends who have supported me along the way.

Table of Contents

CHAPTER 1: Introduction	1
1.1 Motivation	1
1.2 Background	3
1.2.1 Functionally Graded Materials	3
1.2.2 Design of FGMS: <i>Gradient Architectures</i>	6
1.2.3 Processing of FGMS	10
1.2.3a Processing-induced Thermal Stresses	10
1.2.3b FGM Processing Methods	13
1.2.3c Modeling of Processing-induced Thermal Stresses	17
1.3 Objective	19
1.3.1 Scope of Research	19
1.3.2 Contributions of the Research	22
CHAPTER 2: Fabrication of FGMS using Pressureless Sintering	24
2.1 Powder Preparation	24
2.1.1 Powder Selection	24
2.1.2 Powder Mixing	26
2.1.3 Thermal Matching Process	28
2.1.4 Binder Addition	30
2.2 Sample Preparation	31
2.2.1 Square Cross-Sectional Geometry	32
2.2.2 Circular Cross-Sectional Geometry	42
CHAPTER 3: Modeling the Sintering Behavior of Composites	48

3.1	Porosity Model	48
3.1.1	Porosity Calculation	48
3.1.2	First Theoretical Porosity Calculation	51
3.1.3	Second Theoretical Porosity Calculation	54
3.1.4	Results	57
3.2	Characterization and Modeling of Shrinkage	61
3.2.1	Modeling of Shrinkage	61
CHAPTER 4: Characterization of Gradient Architecture Evolution: Microstructure and Mechanical Properties		66
4.1	Mechanical Properties: <i>Hardness Testing</i>	66
4.2	Microstructural Characterization	71
CHAPTER 5: Validation of Finite Element Model of Shrinkage Stress Evolution in Graded Specimens		77
5.1	Contributions of Porosity to Sintering Model	77
5.2	Validation of Sintering Model	80
5.2.1	Determination of Material Properties During Sintering	81
5.2.2	Comparison of Theoretical and Experimental Shape Profile	82
5.3	Stress Evolution During Sintering	83
CHAPTER 6: Conclusions and Future Work		88
6.1	Pressureless Sintering of Metal-Ceramic FGMs	88
6.2	Shrinkage Model for Predicting the Evolution of Porosity during Sintering	90
6.3	Characterization of Pressurelessly Sintered FGMs	91
6.4	Validation of Porosity Effects in Finite Element Sintering Model	93

6.5 Recommendations for Future Work	94
BIBLIOGRAPHY	96

List of Tables

Table 1.	Powder selection by composite layer.	25
Table 2.	Reduction in layer thickness from different bimodal distributions.	38
Table 3.	Adjusted binder quantities for all layers, including additional 5 and 10 vol % Ni layers.	39
Table 4.	Shrinkage data for each composite layer.	47
Table 5.	Initial, final, and theoretical maximum density values for composites sintered to 1350°C.	50
Table 6.	Initial and final porosities for composite layers sintered to 1350°C.	51
Table 7.	Volume fraction of porosity due to the matrix phase and particle phases based on equation (3-14).	56
Table 8.	Typical Vicker's hardness values for nickel and alumina [34]	68

List of Figures

Figure 1.	Impact of a projectile with an armor package consisting of hard outer material and tough backing material [2].	2
Figure 2.	Armor package created by epoxying nickel and alumina plates together.	4
Figure 3.	Gradient architecture consisting of continuous changing region and discretely layered region, and the length scales related to FGM design.	5
Figure 4.	Initial and final states of metal-ceramic composite created by attaching the materials with a sharp interface [5].	6
Figure 5.	Plot of the effect of the gradient thickness and exponent on the peak level of stress in an FGM [12].	9
Figure 6.	Shrinkage results for FGM prior to (left) and following sintering rate adjustment [25].	15
Figure 7.	Powder processing steps, including the options for powder consolidation [28].	16
Figure 8.	Stress singularity that develops along interface at free surface in an FGM, with σ_{22} being the axial stress, and r/l being the normalized distance away from the free surface [19].	18
Figure 9.	Microstructures of 60 vol % Ni layer with hand mixed (left) and ball mixed powder formulations.	28
Figure 10.	Power law distribution for various gradient exponents.	32
Figure 11.	Multipiece square die with cross-section dimensions.	33

Figure 12. Green 12.7 mm FGM sample with 4 interlayers.	34
Figure 13. Tube furnace used for sintering FGMs.	34
Figure 14. Two sintering cycles used for FGM fabrication.	35
Figure 15. 12.7 mm FGM with 4 interlayers after sintering.	36
Figure 16. Fracture surfaces for shrinkage stress crack (left), and residual stress crack.	37
Figure 17. 25.4 mm FGM with 4 interlayers, after sintering.	37
Figure 18. 12.7 mm FGM with 4 interlayers and bimodal alumina layer.	39
Figure 19. 25.4 mm FGM with 6 interlayers and uniform layer thickness.	40
Figure 20. FGM with 6 total layers of uniform thickness, 12.7 mm thick sample.	41
Figure 21. FGM consisting only of graded region no pure base materials, uniform 3.15 mm layers.	41
Figure 22. Die for circular specimens, with 1 in diameter.	42
Figure 23. Crack-free circular specimen, roughly 38.1 mm, uniform layers.	43
Figure 24. 12.7 mm FGMs with identical distributions to square samples; left has 4 interlayers, right has 6.	44
Figure 25. 25.4 mm FGM with no cracks, 8 layers with uniform thickness.	45
Figure 26. 12.7 mm FGM, with 100 vol % Ni and 80 vol % Ni layers inverted.	46
Figure 27. Symmetric FGM, equivalent to two 12.7 mm FGMs attached at the nickel layer.	46
Figure 28. First theoretical porosity model, assuming all porosity is associated with the matrix.	52

Figure 29.	Second porosity model attributing an amount of porosity to the matrix equivalent to that of the pure material, and all remaining porosity associated with the particles.	54
Figure 30.	Plot of the measured and predicted values for the porosity, based on the two theoretical models.	58
Figure 31.	Plot of the calculated difference in porosity between initial and final values from the measured values and the two theoretical models.	60
Figure 32.	Shrinkage data from sintering experiments for each composite material in eight-layered graded material.	62
Figure 33.	Measured shrinkage values for the three nickel matrix layers, along with the curves predicted by the shrinkage model.	64
Figure 34.	Value of coefficients for each volume fraction of nickel in the shrinkage model.	65
Figure 35.	Vicker's microhardness values under 1000g load for each composite layer, including both unimodal and bimodal alumina for the 0 vol % Ni.	69
Figure 36.	Microstructures for each composite material fabricated, labeled by percentage of nickel in the composite.	74
Figure 37.	Microstructures from powder processed FGMs and consolidated by HIP [21].	76
Figure 38.	Shape profile for eight-layered FGM, with bottom three layers consisting of 60, 80, and 60 vol % Ni, from finite element model (left), and fabricated sample (right).	83

Figure 39. Outlines of shape profile for FGM sample and finite element analysis results, using digitizing software.	83
Figure 40. Stress distribution for 25.4 mm thick FGM with eight layers, and the 100 vol % Ni layer replaced by a 60 vol % Ni layer; % Ni content listed for each corresponding layer.	84
Figure 41. FGM without 80 vol % Ni and 100 vol % Ni layers%; Ni content listed for each corresponding layer.	85
Figure 42. FGM fabricated without 80 vol % Ni and 100 vol % Ni layers, preventing fracture during sintering.	85
Figure 43. Stress Distribution at 560°C for 12.7 mm square geometry FGM with eight layers distributed with the labeled nickel volume content.	86
Figure 44. 12.7 mm square geometry FGM with eight layers following fabrication, with a crack in the 60 vol % layer; the location of the maximum stress in the model.	86

Chapter 1: Introduction

1.1 Motivation

With the development of more advanced projectiles, better and more reliable armor packages must be developed in order to absorb their energy, and, if possible, stop them before they damage a target. Projectiles often are designed with a sharp point that delivers the force onto a very small area, creating large stress concentrations and leading to penetration of the surface. A good armor package, thus, has two main functions: 1) to blunt the tip of the projectile to distribute the impact over a larger area and introduce a shock wave into the projectile to break it apart prior to complete penetration, and 2) to absorb the energy of the impact [1].

In order to accomplish the task of blunting the projectile's tip, a hard material is necessary, while a soft, ductile material is necessary to absorb the energy of the impact, as shown in Figure 1. Hence, a metal-ceramic system can be used in an armor package. The problem with a standard system of this kind is combining the materials for optimal stress propagation properties. When a metal plate is joined with a ceramic plate, an interface between the plates will exist, and will prevent stresses from propagating between the two materials in such a way as to optimize performance. Specifically, when a stress wave propagates as the result of an impact through the interface, it creates a tensile force as the wave transmits across and reflects off the interface. Since the sharp interface between the two dissimilar materials is the weakest point in the system, the stresses can lead to debonding of the plates and a reduced ability to absorb the energy of impact.

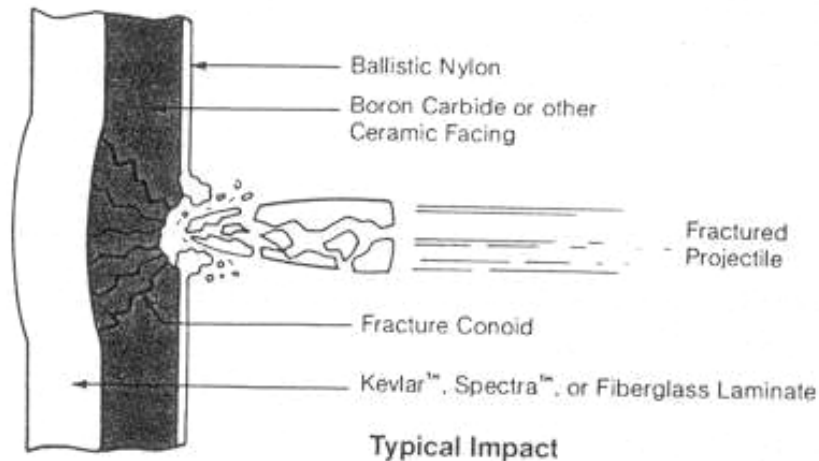


Figure 1. Impact of a projectile with an armor package consisting of hard outer material and tough backing material [2].

One way to control the stresses at the interface is to gradually vary the composition there. This grading would turn the metal-ceramic armor system into a concept known as a “Functionally Graded Material (FGM)”. This concept has already been demonstrated to introduce a ‘time-delay effect’ into the armor package that can delay the time at which the peak stresses that cause tensile fracture will occur at the interface [3].

The potential for graded materials to provide enhanced armor systems provides the foundation for this research. However, graded materials are more difficult to fabricate than simply adjoining two plates together. This research effort seeks to understand the stresses that evolve during fabrication of FGMs, specifically the process of pressureless sintering of metal and ceramic powders, and ways to mitigate them through experimental and theoretical design. Focus is placed on pressureless sintering because it is a more affordable manufacturing technology than alternative powder processing techniques, like Hot Isostatic Pressing (HIP), and requires less preparation of the component (e.g., no protective container for pressureless sintering).

1.2 Background

1.2.1 Functionally Graded Materials

FGMs are a type of composite material classified by their graded structure. Specifically, an FGM typically consists of a composite material with a spatially varying microstructure designed to optimize performance through the corresponding property distribution. Property distributions are found in a variety of common products that must have multiple functions (i.e., multifunctional), such as gears, which must be tough enough inside to withstand the fracture, but must also be hard enough on the outside to prevent wear. Gear teeth are in constant contact, and therefore their surface hardness becomes of primary concern to prevent them from deteriorating during use [4]. However, if this factor were the only considered design criterion, the gear may suffer from fracture under the constant loading since hardness and toughness are mutually exclusive. Similarly, a turbine blade also possesses a property distribution. Again, the blade must be tough to withstand the loading it is subjected to, but it must also have a high melting point to be able to withstand high temperatures on the outer surface [4]. As with hardness and toughness, these different material properties tend to mutually exclude one another.

One method to overcome the exclusivity of these properties is to combine multiple materials together, such as metals and ceramics in situations that call for both toughness and hardness or heat resistance. This is the approach taken for armor applications, which have requirements that most closely resemble those for gears. For armors, ceramics are used as a hard outer surface to resist impact, while metals are used

as a tough inner surface to absorb energy. A traditional method to create a metal-ceramic armor package would be to simply combine two plates together with an adhesive, such as is shown in Figure 2. However, when simply combining two materials like these together, additional issues arise, such as weak interfaces and large differences in other properties, such as thermal expansion [5].

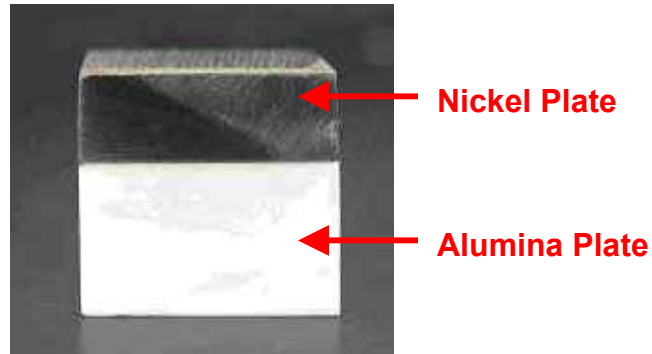


Figure 2. Armor package created by epoxying nickel and alumina plates together.

A graded interface rather than a sharp interface between two dissimilar materials, thus, defines graded materials. The graded interface in these materials is a series of changes in the microstructure of the composite that can be created in discrete layers or as a continuously changing system, and is known as the *gradient architecture*. Figure 3 illustrates both continuously and discretely layered functionally graded materials, as well as the size scales the on which the features are present. In this figure, material 0 represents the nickel, and material 1 represents alumina, with the graded region between the two materials. The properties of the composite change as the relative amounts of the constituent materials vary with respect to one another. In many cases, the property distributions can be described by rule-of-mixtures (ROM) [6,7] and modified ROM calculations [8-10].

Using a graded microstructure minimizes the differences in properties from one material to another. On a local level, if the gradient is smooth enough, it may appear that there is no change in the microstructure. Having a smooth transition limits the property mismatches from one point in the material to an adjacent one. Hence, in an ideal functionally graded material, there is no longer a sharp interface, and as a result, no single location that is inherently weaker than the rest of the composite. The removal of the weak interface is one of the most important reasons for designing FGMs, because its presence prohibits the functionality of the material from being addressed.

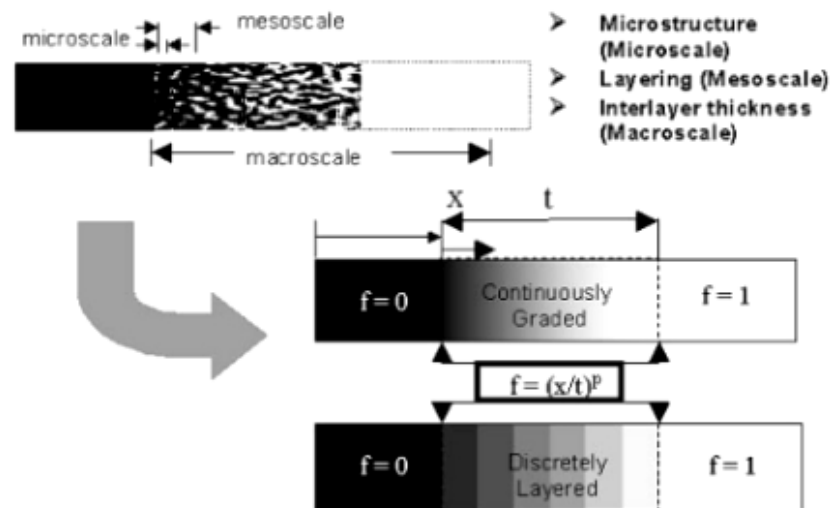


Figure 3. Gradient architecture consisting of continuous changing region and discretely layered region, and the length scales related to FGM design.

When attaching two dissimilar materials together, mismatches occur that reduce the integrity of the composite. For example, if one material is used as a coating on a different base material, differences in the thermal expansions of these materials may cause additional stresses that can lead to overall failure of the component. Similarly, if two materials are joined at an interface and are subjected to an axial impulse loading, as in armor applications, a stress wave will propagate through the materials as described by Meyers [11]. The propagation of stress waves through graded materials has been studied

in one, two and three dimensions in previous work [12,13]. As the stress wave from impact reflects and transmits across the interface, a tensile force will appear that can lead to debonding along the interface. If the joined materials are used in an energy absorbing system, the ability to absorb energy will be compromised when the system fails.

1.2.2 Design of FGMS: *Gradient Architectures*

The fabrication of composites with a sharp interface is difficult due to the variation in properties between the base materials. During fabrication of this type of composite, the differing properties between the materials can lead to large stresses. These stresses may result from the large differences in thermal properties or any other residual stresses that exist in the system when the materials are combined and processed, as shown in Figure 4. Either of these cases can lead to fracture in the composite and are important factors in determining the fabrication processes and materials used in the composite. However, when considering applications of the composite system, there are additional factors that influence the desirability of FGMS over the traditional composite system with sharp interfaces.

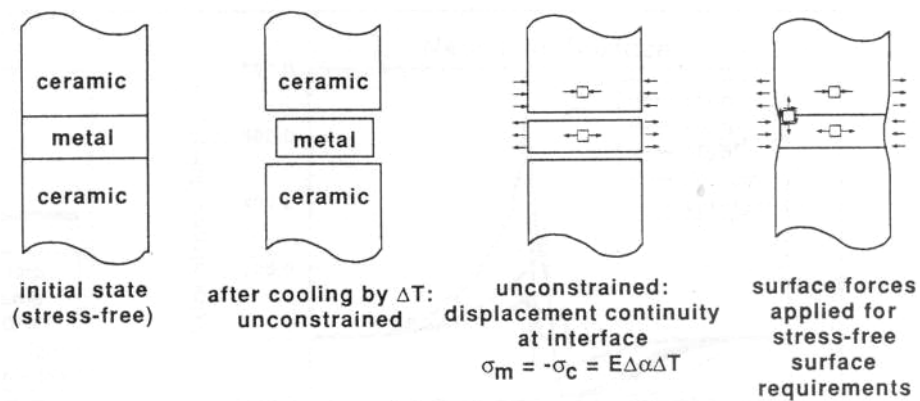


Figure 4. Initial and final states of metal-ceramic composite created by attaching the materials with a sharp interface [5].

As previously mentioned, it has been shown that a graded interface can influence the evolution of stresses propagating through a metal-ceramic armor package by introducing a time delay benefit that can improve the armor's resistance to failure [3]. In a composite armor package with a sharp interface, a tensile force arises at the interface as a result of the stress waves from the impact. Due to the inherent weakness of the interface, the tensile force can lead to fracture, preventing the optimal energy absorption from the armor system. However, in a layered FGM, the reflections and transmissions of the initial stress wave will interact with each other from each interface in a material, eventually leading to fracture when the peak stresses are in phase at an interface. Delaying the time it takes to reach this peak stress delays the initiation of damage and improves the energy absorption ability of the material. The most important aspect of an armor package related to the removal of energy from the impact is due to the loss of mass of the projectile [2,14]. If the interfaces in the armor system fail prior to a sufficient dissipation of energy, the system could be penetrated. Hence, the time-delay benefit of the gradient architecture that is used in the design of the FGM armor package provides an important functional characteristic.

There are often many ways to design a gradient architecture, which are constrained by the materials involved and the intended use of the composite. A number of methods to describe the gradient structure are given by Markworth, et al. [15]. One method often used in designing material gradients is the power law distribution, introduced by Kawasaki and Watanabe [16,17]. The power law in equation (1-1) is useful because it allows the composite to be tailored to specific uses.

$$f_0 = \left(\frac{x}{t} \right)^p \quad (1-1)$$

Adjusting the exponent, p , controls the rate of transition between microstructures of base materials 0 and 1 in Figure 3 with f_0 being the volume fraction of material 0. The power law distribution is a versatile tool, as it can be used to fabricate a wide variety of distributions. As the exponent becomes much larger or much smaller than one, the gradient tends to be smoother near either of the base materials. Additionally, a gradient exponent of one creates a linear distribution. For instance, in a general metal-ceramic material system, if a harder material is needed, the gradient can be designed for a gradual change in the microstructure of the ceramic regions, with a more rapid transition in the metallic portions of the composite.

Choosing the proper exponent for a particular functionally graded material is necessary for not only the intended material function, but also for stress reduction during fabrication. Previous research has modeled the evolution of residual stresses and strains that exist during cooling immediately following the densification of functionally graded materials [16,18-20]. Furthermore, models have shown that graded interfaces can reduce the stresses that evolve during this cooling period. Specifically, research has shown that the stress distribution can be optimized by selecting the proper exponent and by increasing the overall thickness of the graded region of the FGM in a rod geometry [18]. This model determined that designing the proper gradient architecture could minimize the peak stress in the FGM, as shown in Figure 5. By increasing the thickness of the graded region, the stresses can be dissipated more easily. In addition, the exponent can be chosen such that the gradient can be more gradual in the region with higher stress

evolution. Hence, fabrication issues are also important in determining the microstructural transition of the FGM, in addition to the intended uses.

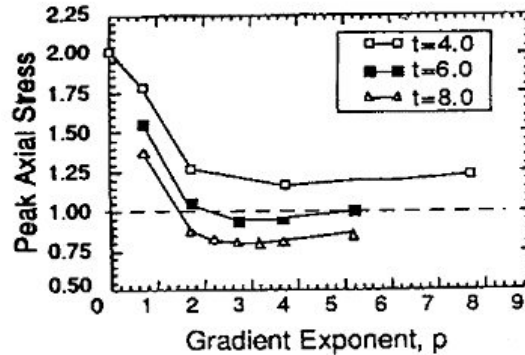


Figure 5. Plot of the effect of the gradient thickness and exponent on the peak level of stress in an FGM [18].

An area of importance in designing FGMs is in describing the properties of the composite system. The rule-of-mixtures is the most common method for calculating properties of a composite material, due to its simplicity. Research by Bruck and Rabin compared these calculations to measured values of the coefficient of thermal expansion and determined that the predictions were suitable for interpenetrating phase microstructures, but the damage present in particle-reinforced structures required the development of a new ROM calculation [9]. The new ROM was used to evaluate the damage in particle-reinforced composites through measurements of their elastic moduli [10]. Additional property models have focused on the micromechanics of the FGMs [21] and the interactions of particles and matrix [22] by considering a representative volume element that is assumed to predict the bulk material properties.

1.2.3 Processing of FGMs

Much of the previous research mentioned has dealt with benefits of continuously graded structures. However, the fabrication of these types of graded materials has inherent problems associated with it. In order to produce a continuously graded structure, costly fabrication methods are necessary. On the other hand, by reducing the graded region into a number of discrete layers, the material can be fabricated more easily. Research has demonstrated that an optimal number of discrete layers can be fabricated in an FGM with no adverse repercussions in the material's properties [3,23]. Layering techniques offer the ability to build up the graded region incrementally, which can be done without sophisticated equipment to continuously monitor the microstructure. Layering processes require only a quantity of material to be known, because that material is simply added on to other material. Continuous grading is not as simple, because materials must be continuously added, and the amounts are always changing. Materials can be gathered together and then layered in a desired manner without continuous monitoring. In order to use a similar procedure in a continuous structure, an infinite number of material mixtures need to be prepared. As long as a discretely layered FGM provides benefits over a composite with a sharp interface, as modeling studies have shown [3,15,16], though, then they are suitable for use in material systems.

1.2.3a Processing-induced Thermal Stresses

When creating a layered composite, problems arise due to the different material properties between adjacent layers. Each layer will react differently to various loads due to the different amounts of base materials present. These variations in thermomechanical

responses result in stresses at the interfaces of the layers [24]. Previous FGM fabrication work demonstrated that each layer shrinks during sintering and cooling at different rates and in different amounts resulting in large relative deformations in the sample between layers [25,26], and causing loads at the interface that can sever the composite. If the differential shrinkages occur prior to the material's fracture toughness becoming strong enough to withstand the stresses, the composite will be unable to consolidate crack-free.

The differential stresses between adjacent layers are influenced by more than just the differences in the thermomechanical properties of the composite. The geometry of the FGM also has an effect on the stress evolution and fracture behavior of the composite. For instance, due to the initiation of fracture at the intersection of free surfaces and interfaces, fabricating a layered graded material with sharp corners will induce stress concentrations at those locations that will increase the likelihood of crack growth. As mentioned before, differential stresses lead to debonding, and interfaces are highly susceptible to these types of failures. When geometrical effects, such as sharp corners, are introduced, stress concentrations can enhance the weakness of the interfaces, because they provide an initiation site for cracking. It may be possible, though, to mitigate these effects by fabricating different geometries for the FGMs, such as circular geometries. In an axisymmetric composite, there are no longer locations on the free surface of the composite where stress concentrations will build up easily. However, circular geometries cannot be used in armor applications, since they cannot provide a modular system without any gaps. Thus, it is necessary to find a way to minimize the stresses at corners while also allowing for a modular armor package.

During fabrication of the functionally graded material, the material is subjected to possible failure-inducing stresses at different times in the sintering cycle. During the initial heating stage, when the composite undergoes consolidation, the different layers in the FGM are prone to cracking due to the low fracture toughness of each composite interlayer. Since the graded material begins as a powder compact, it does not yet possess the material properties of the fully dense composite. Rather, the properties must evolve during sintering. This evolution, though, leaves the material susceptible to failure, since the differential stresses cannot be withstood by the weak fracture properties of the interfaces. As a result, when the amount of shrinkage begins to vary greatly between adjacent layers, and the stresses build up, the graded material is likely to fracture as a result of sintering stresses.

On the other hand, once the composite has reached the final sintering temperature and it undergoes maximum consolidation, it must be cooled back down to room temperature. During this portion of the sintering cycle, residual stresses that have accumulated during sintering cause cracks to form due to differences in the coefficient of thermal expansion. Previous modeling work has been done to study the effect of graded distributions on the residual stresses in a functionally graded material [16,18]. The main difference between the heating and cooling stresses are related to the amount of consolidation of the material and the related strength, in addition to the presence of residual stresses during cooling that are not present in the heating cycle. In the residual stress modeling, the properties of the materials are based upon fully dense materials with predictable properties, for example in Rabin and Bruck [19]. These properties can be interpolated between temperatures to understand the behavior of the material throughout

cooling. Shrinkage stresses are not as predictable though, because the properties are not based on the fully dense material, but rather they evolve as the material densifies.

1.2.3b FGM Processing Methods

There are a number of methods to process FGMs. Some layering methods include powder processing techniques, coating processes, and lamination processes [4]. These are constructive processes, because the composite material is literally constructed in a series of layers. Additionally, there are different types of fabrication methods, such as transport-based processes that are based upon the principles of thermal and mass transport. Constructive processes are fairly simple and can produce a layered graded material with any number of distributions.

There has been a lot of work done regarding the fabrication of FGMs using various layering processing approaches that have been discussed by Suresh and Mortensen [4]. Some layering approaches that have been used to fabricate FGMs are powder processes, as well as coating processes such as thermal spray deposition and electrodeposition. Coating processes are so named since they typically begin with a base component and build a gradient onto that component for protection from the conditions of use. In thermal spray deposition, a melted metal is sprayed onto the base component where it quickly solidifies to build up the gradient, creating a composite that is almost fully dense. Solid reinforcing particles can be included in the metal, but one of the drawbacks is that the reinforcement can only be included up to a volume fraction where the particles remain in the molten metal [4]. Hence, it may be difficult to create a complete gradient between two base materials, especially if one of the materials is a

ceramic with a high melting point. Other coating processes have disadvantages related to the nickel-alumina material system desired for armor applications in this research, as well. For instance, electrodeposition can be used to create a continuously graded architecture, however, as with thermal spray deposition, the amount of reinforcing particles is limited [4]. Additionally, the amount of time to create a sufficiently thick gradient for use in an armor package would be excessively long, as research has demonstrated “a total processing time of 30 days for a coating thickness of 80 μm [4,27].”

Powder processing techniques are good for functionally graded material fabrication because they are fairly quick and cheap. No expensive equipment is necessary, and only a few items are required for fabrication. The only material necessities are material powders that form the basis of the composite material system. These materials are mixed together in various concentrations to create the desired composites. Powder processing allows for good microstructural control of the final material by mixing different amounts of the base powders, and by using different particle sizes of the constituent materials [28]. Additionally, the composition of the graded material can be controlled easily due to the layering techniques of each of the powder mixtures. Powder processing techniques also allow for shape-forming capability. Since the powders do not begin in a solid geometry, they can be placed into a geometrical die and pressed into a desired shape.

On the other hand, though, there are some problems associated with powder processing. One problem with powder processing is the limitation on the thickness of the layers that can be produced [4]. The most notable problem is overcoming the

differences in sintering properties, as discussed earlier. Some different approaches can be used to alleviate these difficulties, such as differential temperature sintering which aims to control the sintering behavior by adjusting the temperatures in specific regions, whereby the materials will sinter at the rates for that temperature. Also, there are methods that are aimed at controlling the material's behavior through processing prior to sintering [25,29]. Specifically, these approaches control the shrinkages and sintering rates, as shown in Figure 6, by altering the green density (i.e. the density of the unsintered compact) and porosity in the unconsolidated compact. Methods that control the material behavior through processing are more desirable when they can be applied, because they are easier to use and do not require additional equipment.

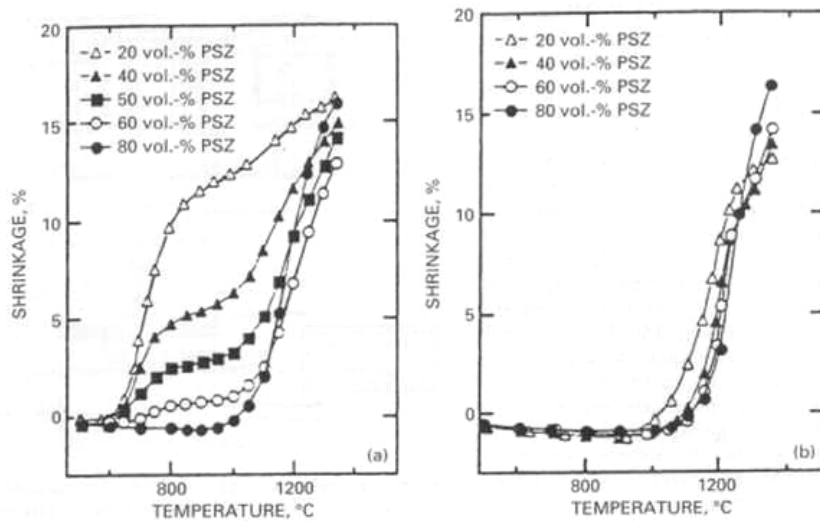


Figure 6. Shrinkage results for FGM prior to (left) and following sintering rate adjustment [25].

There are numerous methods for use in consolidating the functionally graded compact, as shown in Figure 7. Some previous research has fabricated graded materials using hot pressing and hot isostatic pressing (HIP) [28,29]. Hot pressing and HIPing both apply pressure to the sample during the heating cycle. The external applied pressure

helps to restrict deformation alleviate the stresses that lead to fracture. During hot pressing, reactions have been seen between the sample and the die at high temperatures [28]. On the other hand, HIPing requires a lot of work to prepare samples before they can be heated. Thus, for very large samples, a procedure such as HIPing would be awkward and difficult, and would increase the costs associated with fabrication.

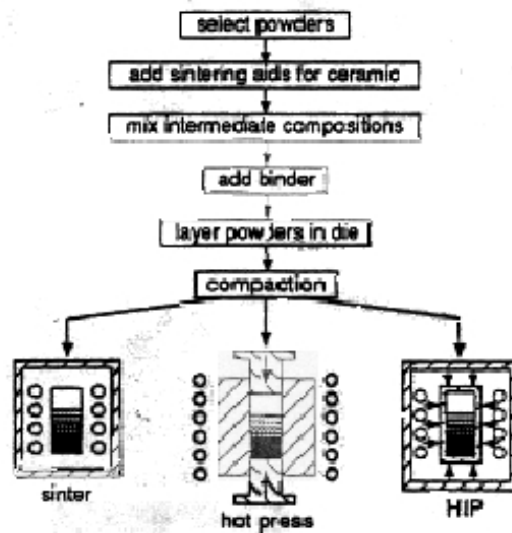


Figure 7. Powder processing steps, including the options for powder consolidation [28].

Another method to consolidate the composites is pressureless sintering. Pressureless sintering requires a high temperature furnace, but does not need any preconditioning of the materials. Depending on the material system used, an inert atmosphere may be necessary to prevent oxidation, but that can be provided without any material preparation. Due to the lack of preconditioning of the functionally graded material, there are less time and cost requirements. Although, since there is no external pressure applied to the sample, there is no restriction on the deformation behavior of the material, and there is no force to mitigate the differential stresses between layers. However, pressureless sintering remains a desired densification method due to its low

cost and ability to produce a wide variety of geometries. Furthermore, pressureless sintering does not typically remove all of the porosity during consolidation, which is beneficial in an armor package. There has not been any previous research, though, into the fabrication of functionally graded materials with a nickel-alumina material system through pressureless sintering in geometries more complex than rod geometry. This nickel-alumina system has been successfully fabricated in a graded material using HIPing [29], but pressureless sintering provides an easier method to consolidate the materials.

1.2.3c Modeling of Processing-induced Thermal Stresses

Some prior research has been focused on the evolution of stresses during sintering in order to provide a method for optimizing the design of FGMs [30-32]. These studies were based upon a viscoplastic model that uses average properties and stresses within the FGM. These models do not focus on the affect of particles in a reinforced matrix structure.

In other research, models have been developed to study the effects of thermal residual stresses in the composites following sintering, as well as how to mitigate the stresses through graded interfaces [5,16,18,20]. In fully dense materials, the residual stress distributions are modeled based upon the known properties of the materials at different temperatures. In these previous efforts, it was determined that the residual stresses can be reduced through controlling the gradient and thickness of the FGM. Specifically, the modeling showed that the type of distribution and thickness of the graded region can be optimized for a given material system [18]. Having the ability to

optimize the graded composite is important, because in most applications, any crack that develops would render the composite useless.

In addition to the gradient optimization modeling, some work has also been done on the geometrical effects on stress distributions [20]. This research focused on edges and interfaces and the stress concentrations that developed at these locations, as well as the two- and three-dimensional effects on the stresses. There is a large stress singularity that builds up at the sharp corners on the free edges of the composite, as well as at the interfaces of the different layers in the graded region. This singularity has been modeled and is shown in Figure 8. These stresses provide initiation sites for cracks that can quickly lead to failure depending on the strength of the interfaces, or the toughness of the materials.

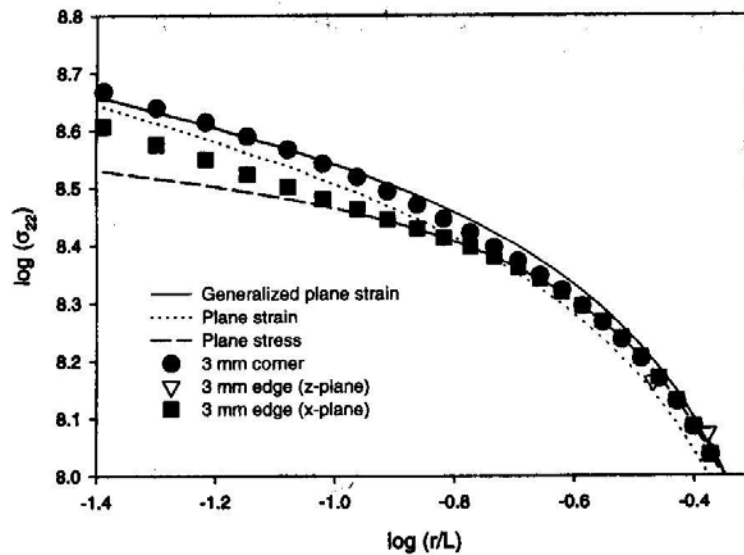


Figure 8. Stress singularity that develops along interface at free surface in an FGM, with σ_{22} being the axial stress, and r/l being the normalized distance away from the free surface [20].

1.3 Objective

The objective of this research is to fabricate functionally graded materials without cracks in modular geometries through pressureless sintering of metal and ceramic powders. Also, models are created to illustrate the evolution of stresses during sintering to predict the ability to fabricate FGMs for armor applications without crack formation.

1.3.1 Scope of Research

The research covers the aspects of fabricating the graded materials using pressureless sintering and modeling the stresses that evolve due to shrinkage. Chapter 2 focuses on the processing work used to fabricate the FGMs. Initially, the FGM's were fabricated using the findings from the previous research on HIPing [29], and incorporating gradient architectures thought to provide lower stresses. The basic powder processing techniques applied were outlined in previous research [28]. Many of these architectures were tried without knowledge of whether or not they had a good chance of providing crack-free samples.

Many approaches are discussed in Chapter 2 with these focusing mainly on gradient architecture and FGM geometry. Furthermore, the application of different particle-sized powders and the addition of a polymer binder are discussed. The different particle sizes and the organic binder are part of a thermal matching approach to FGM fabrication. In this chapter, this approach is presented and its applicability towards the present scenario is discussed.

The modeling work performed in this research is described in Chapter 3. The focus of the models is the sintering behavior of the nickel-alumina composites.

Specifically, in Chapter 3, models are presented to describe the porosity of the FGM layers, the stress evolution of the nickel-alumina FGM as it pertains to fabricating crack-free armor specimens, and the shrinkage rates of each layer with respect to the temperature.

The porosity model discussed in Chapter 3 describes the calculations that are used to calculate the amount of porosity consumption. These calculations are important in understanding and overcoming the differential shrinkage problems. An interlayer that does not remove as much porosity during sintering will not experience as much shrinkage as adjacent layers that consume much more porosity. These models do not solve the problem of differential shrinkage, but their ability to locate the problem areas are important and are discussed in the chapter.

Since the material evolves as the temperature increases from a powder compact to a fully dense composite, the sintering rate also evolves. The second model presented in Chapter 3 deals with modeling the shrinkage rate of the composite interlayers during sintering. The relationship between the temperature and the sintering rate was studied because of its importance in finite element modeling. The ability to be able to predict the shrinkage rate allows the modeling of material systems without a lot of initial material testing. No prior research has been found that examines the shrinkage of materials that begin as a powder compact and sinter into a fully dense structure.

In Chapter 4, the focus of the work shifts to the characterization techniques used to describe the FGMs. In this chapter, the hardness testing applied to the FGMs after processing is presented. The hardness tests focused on quantifying the consolidation of the materials in a manner that focuses on porosity, rather than just the change in volume.

The characterization of the hardness values is useful in determining how the properties of different mixtures of powders vary as a result of sintering. This property information could be useful not only in models, but also used simply as a method for inquiring into how materials processed and then that data could be used for inclusion in a sample.

Additionally, in Chapter 4, the microstructural observations made are discussed and related to FGM processing. Specifically, the observations are used to compare fabrication techniques, including mixing techniques and sintering results. The observations allow for problems that prevent consolidation, such as the formation of particle agglomerations, to be addressed. Furthermore, these observations are necessary in order to validate the assumptions made in the development of the finite element model developed in Chapter 5.

A finite element model is presented in Chapter 5 that models the stresses that evolve during sintering. A description of the model is given, and the assumptions included in the model are discussed. The finite element model provides the ability to predict the stresses that are produced for the desired geometry and gradient architecture. This model allows for the determination of viable gradient regions prior to the fabrication of the actual composite. The model uses porosity inputs to determine the material property evolution, which can be used to calculate the stresses. The use of finite element modeling saves time because it eliminates the need to actually fabricate each different graded sample. In Chapter 5, the validation of model is presented based upon qualitative and quantitative comparisons with actual FGM specimens.

1.3.2 Contributions of the Research

The unique contributions of this research are the models for the evolution of the sintering rate with temperature, as well as the finite element modeling of the stress evolution during the heating portion of the sintering cycle. Earlier sintering models have relied on a viscosity model assuming average properties and stresses in the FGM. The current model applies reinforced matrix assumptions based upon Mori-Tanaka and Eshelby models. Additionally, the model is compared with fabricated specimens to validate the stress profile with respect to FGM fracture. The model is useful for predicting the location of maximum stresses, and the geometries and distributions that are likely to be fabricated without fracture. While it was not feasible to measure the stresses that occurred in the fabricated FGM specimens in the current research effort, the model is capable of providing the locations of maximum stress where failures are most likely to occur in fabricated specimens.

Furthermore, the fabrication of FGMs is studied through the use of pressureless sintering. Past research efforts have not focused solely on consolidation by this method, but have instead only used this method in comparison with other technologies that apply external pressure to the sample during sintering. Having the ability to fabricate FGMs without the addition of external pressure is useful in reducing the time and cost of manufacturing these composites.

In addition, prior research utilizing pressureless sintering in the fabrication of FGMs has not focused on the applications of armor packages. As such, the geometries of these fabrication efforts have dealt mainly with circular cross-sections. However, with a focus on armor in this research, more complex geometries (i.e. cross-sections that can be

assembled modularly) must be fabricated. The distortions and cracks that develop during pressureless sintering of FGMs become a larger issue when fabricating armor specimens.

Chapter 2: Fabrication of FGMs using Pressureless Sintering

In this chapter, a procedure for fabricating FGMs through the pressureless sintering of metal and ceramic powders is described. First, the selection and preparation of the powders is discussed. Then, the preparation of specimens with square and circular cross sectional geometries is presented. The steps are similar to the process outline by Rabin and Heaps [28], however, the focus is on pressureless sintering and overcoming the fabrication problems that result from this method of consolidation.

2.1 Powder Preparation

The preparation of the composite mixtures used in the creation of functionally graded materials follows a typical process of powder selection, powder mixing, and when necessary, the addition of an organic binder. The details of these processes are discussed herein.

2.1.1 Powder Selection

In order to create a layered functionally graded material through powder processing, individual powder mixtures must be fabricated. The graded material consists of the base materials on either end, in order to achieve the desired properties, with a region connecting these layers consisting of mixtures of the base materials. Mixing the constituent materials together in various relative amounts, depending on the desired distribution, creates these intermediate layers.

When certain mechanical properties are desired for a given material, the microstructure plays a strong role in determining the specific particle sizes for each

powder used in a composite mixture. In the case of armor applications, the desired properties vary from a hard outer material to a tough inner material. In previous work, use of different particle sizes in various composite mixtures showed the various microstructures created [10]. In order to create a matrix material with discrete particle reinforcement, it is necessary to use a small particle powder for the matrix phase and a large particle reinforcing phase material, as shown in Table 1. Once the percolation threshold is approached, the materials begin to form interpenetrating phases with less desirable mechanical properties.

Table 1. Powder selection by composite layer.

vol % Ni	Alumina		Nickel	
	0.4 μm	18 μm	3 μm	17 μm
0	X			
5	X			X
10	X			X
20	X			X
40	X			X
60		X	X	
80		X	X	
100			X	

Beginning with large and small particle sizes for both nickel powders and alumina powders, the smaller particle-sized powders are chosen for the composite mixtures where that material is the largest constituent and forms a matrix phase. The larger particle powders are incorporated for the secondary, reinforcing phase. These situations refer to when the material does not comprise the majority of the mixture.

The composite layers are distributed based on the percent of each material present by volume. In order to calculate how much of each powder to use, the following equations are used:

$$(m_{Ni}) \left(\frac{1}{\rho_{Ni}} \right) = V_{Ni} \quad (2-1)$$

$$\frac{V_{Ni}}{v_{fNi}} = V_{Total} \quad (2-2)$$

$$(1 - v_{fNi})V_{Total} = V_{Al_2O_3} \quad (2-3)$$

$$(V_{Al_2O_3})(\rho_{Al_2O_3}) = m_{Al_2O_3} \quad (2-4)$$

The first equation calculates the volume of nickel, V_{Ni} , from a given weight of nickel powder, m_{Ni} . The next equation determines the total volume of the composite, V_{Total} , based on the volume of nickel and its volume fraction, v_f . Finally, the volume of alumina powder, $V_{Al_2O_3}$, necessary is determined and converted into the weight of alumina powder, $m_{Al_2O_3}$. These calculations allow powder to be weighed rather than measured volumetrically to create the composite mixtures. Using volumetric measurements does not provide good enough accuracy of the powder present without complete compaction of the powder to remove all of the voids present.

2.1.2 Powder Mixing

Once the selected powders are weighed out for a specific composite layer, the powders must be thoroughly blended together to ensure the maximum dispersion of the particles for optimal mechanical properties. In order to achieve discrete particle-reinforced microstructures, the reinforcing phase must be spread out throughout the matrix phase. After being weighed out to the designated amounts, the powders are poured into a single glass jar and the lid is closed tightly. The first method for blending the powders is shaking the dry powders by hand. This mixing technique is accomplished by repeatedly shaking the jar back and forth at about 1 Hz for ten minutes.

One problem with this technique is that it is difficult to maintain for extended periods of time, thus making it difficult to determine if the powder has been adequately mixed. Additionally, since this method relies on human power, it is limited in its ability to separate groups of particles that have stuck together, because there is a limited force applied to the powder.

Another mixing method involves placing the jar of material onto a tumbler to rotate the jar at 60 rpm. Included in the jar with the powders are fifteen 0.5 inch glass balls to help distribute the powders. The problem with this technique stems from the powder's desire to reach a state of minimal energy. The powder mixture has a tendency to slide along the bottom surface of the jar as the jar rotates, rather than fall off of the side of the jar onto the powder below once it reaches a critical height. The glass balls offer some help in stirring the powder, but they, too, roll along the side of the jar and cannot thoroughly blend the powder mixture.

The hand shaking method was the technique used originally for mixing the powders; however, due to the problems discussed above, significant particle agglomeration occurred with the 18 μm alumina powder that inhibited the ability to create a discrete particle-reinforcement, as seen in Figure 9. Additionally, the inability to fully break up and distribute the agglomerations impedes the composite's capability to fully consolidate during sintering.

The ball mixing technique was incorporated in response to the agglomerations observed in the hand shaken powders. The ball mixing technique helped to disperse some of the particles and improve the sintering results, measured by the amount of shrinkage of a disk of the material, by 25%. The shrinkage of the diameter of the disk

increased from 6.34% to 7.95% as a result of the ball mixing process. However, an examination of the microstructure of the ball mixed powder in Figure 9 reveals that there remains some particle agglomeration in this disk, although it is less than that in the hand shaken powder. The ball mixing technique was applied to all powder mixtures following the results of the experiment with the 60 vol % Ni powder.

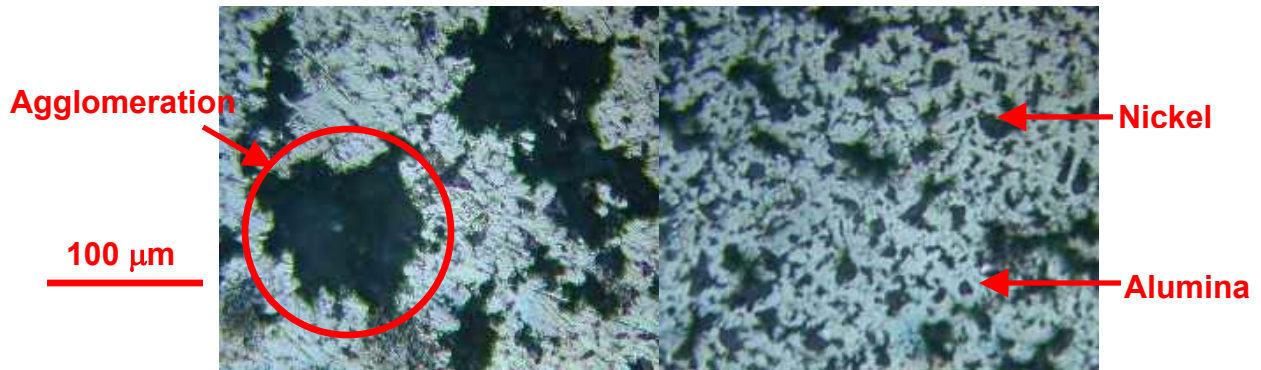


Figure 9. Microstructures of 60 vol % Ni layer with hand mixed (left) and ball mixed powder formulations.

2.1.3 Thermal Matching Process

The thermal matching process is designed to minimize the shrinkage stresses that develop in the graded material by matching the green properties of a layer to its sintering behavior and to the sintering behavior of the surrounding layers. Previous work described the successful thermal matching of nickel-alumina graded plates while using HIPing as the consolidation method [29]. The thermal matching process helps modify the green density of each layer of the FGM in order to more closely match the sintering temperatures and sintering rates of all of the layers. Differences in the sintering temperatures cause stresses to evolve because the layers will begin to shrink at different points during the thermal cycle, leading to layers starting to shrink when the fracture toughness is very low due to inadequate consolidation. Furthermore, the sintering rates

compound the problem of differential shrinkage stresses since the layers will be shrinking at different rates relative to one another.

One of the methods of controlling the properties of the graded layers is through the addition of various quantities of a low-density polymer binder. The binder is already useful in the ceramic-rich layers for its ability to maintain cohesion in these regions. The nickel-rich layers have less need for a binder for this reason, since the nickel is more ductile, and can be compacted under pressure into a cohesive green sample. In the thermal matching process, the binder is helpful because it alters the green density of the composite mixture, allowing for better matching of the powder layers. Additionally, the binder introduces additional porosity into the composite layers once it is burnt out at a low temperature early in the sintering process. The additional porosity creates voids for the powder to consolidate into, allowing for greater shrinkage results in the powders during sintering. By determining the proper amount of binder to include in a given layer, the shrinkage of that layer can be altered in order to match its shrinkage results with that of the neighboring layers.

While the variation of binder in the green compacts can impact the sintering results of the layers, the particle sizes selected for use in the layers also has a significant impact on the stresses that develop in the FGM. As discussed previously, the particle sizes of powders chosen for any given composite layer has a lot to do with the desired microstructure of that layer. However, by selecting different particle sizes, or different particle distributions, such as bimodal or unimodal, the amount of shrinkage in a layer can be increased or decreased. By controlling the amount of shrinkage, the differential

shrinkages between different layers can be minimized, and thus, the differential shrinkage stresses can be reduced.

Using bimodal distributions in the interlayers can affect the shrinkage, as well. In the interlayers, the goal is to increase the amount of shrinkage in order to more closely match the sintering results of the pure end layers. In order to accomplish this additional shrinkage, a small amount of small particle powder can be included in the large particle reinforcing phases to provide added particles for sintering. However, applying this method for thermal matching incurs the trade-off of altering the microstructure

2.1.4 Binder Addition

The binder addition occurs after the composite powder has been fully mixed. The binder used, Q-PAC 40, is an organic binder delivered to the powder mixture by dissolving it in acetone in a known concentration, $C_{BinderSolution}$. The following calculations are used to determine the amount of binder solution to add to the dry powder:

$$W_{DryPowder} + w_{f\ Binder} W_{Total} = W_{Total} \quad (2-5)$$

$$W_{Binder} = w_{f\ Binder} W_{Total} \quad (2-6)$$

$$W_{Solution} = \frac{W_{Binder}}{C_{BinderSolution}} \quad (2-7)$$

$W_{DryPowder}$ is the weight of the composite powder mixture, w_f the desired weight fraction of binder in the particular composite powder, and W_{Total} is the weight of the powder plus binder. The weight of the binder to be added is then calculated, but must be

converted to the weight of solution to be added to the dry powder, since it is dissolved in solution.

Following the addition of the binder solution to the powder, the acetone must be evaporated out of the mixture. Once the acetone has been fully removed, the dried powder is crushed with a mortar and pestle and sieved to 150 μm in a 60 mesh sieve. This new powder plus binder will be used in the creation of the functionally graded material specimens. Initially, each layer is fabricated with 3.5 wt % binder in the final mixture.

2.2 Sample Preparation

In a continuous functionally graded material, the distribution can be described in a power law function, as previously described in Chapter 1, where V_{Ni} is the volume fraction of nickel, x is the distance from the pure alumina interface, t is the thickness of the entire graded region, and p is an arbitrary exponent that governs the distribution of the graded region:

$$V_{Ni} = \left(\frac{x}{t} \right)^p \quad (2-8)$$

Selecting an exponent greater than one provides a gradual transition of the ceramic-rich region, while an exponent less than one creates a gradual nickel-rich region. An exponent of one produces a linear distribution as displayed in Figure 10. While these calculations dictate the fabrication of a continuously graded component extremely well, they can also be used as a guide in the fabrication of a layered composite. The problem with layered composites is that there can only be a finite number of layers, with a finite

thickness, so the power law distribution can only direct where the chosen layers should be located.

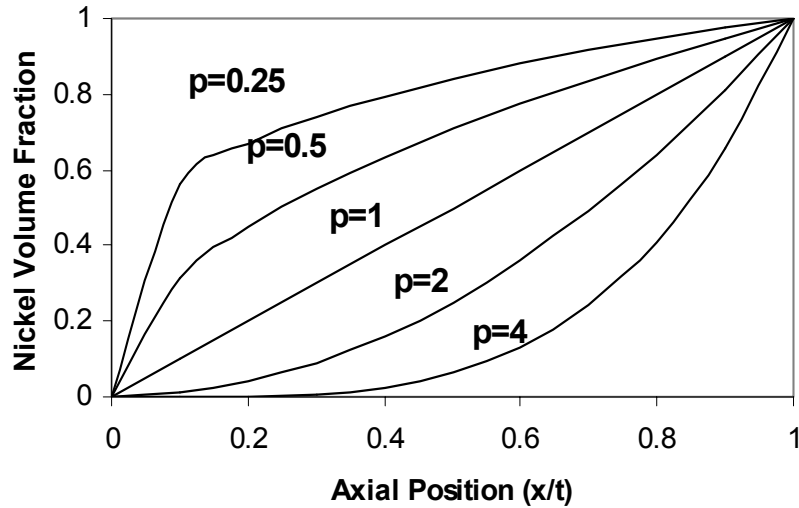


Figure 10. Power law distribution for various gradient exponents.

2.2.1 Square Cross-Sectional Geometry

In this work, a linear distribution was originally selected for a graded region composed of four interlayers: 20 vol % Ni, 40 vol % Ni, 60 vol % Ni, and 80 vol % Ni. While a gradient architecture described by a power law relationship with a gradient exponent of 3 has been shown to minimize thermal residual stresses with as few as four discrete layers [18], there were problems observed with shrinkage stresses during pressureless sintering that motivated the change to a linear gradient architecture. The graded region was the same thickness as each pure base material region - 4 mm. Using the linear distribution, each interlayer has a thickness of 1 mm, for a total sample thickness of 12.7 mm.

In order to determine how much powder is necessary to create the desired thickness of each layer, the geometry of the FGM must be known. In this case, graded

plates with square geometries are preferred for use in armor applications, because they are the simplest modular geometry. Hence, a multi-piece square die is used with the dimensions shown in Figure 11.

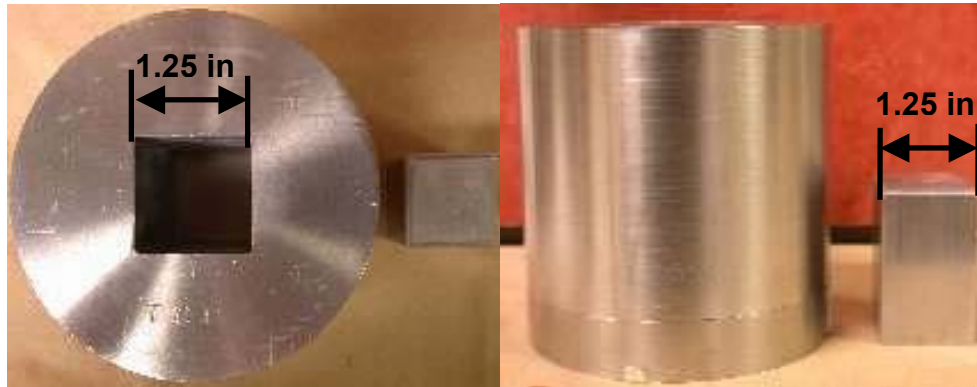


Figure 11. Multipiece square die with cross-section dimensions.

The amount of powder necessary to create a given layer thickness is calculated by the final volume of the layer multiplied by the theoretical density of the composite layer. For this square die, the final dimensions of the layer are calculated based on a final area of 6.25 cm^2 , roughly 1 in^2 , multiplied by the desired thickness. These calculations assume a fully dense specimen after sintering.

Following the powder creation steps discussed earlier, the specimen is layered in the die beginning with the 0 vol % Ni powder. It was found that layering in the die with the pure alumina placed in first made the sample easier to remove following compaction than when the samples were fabricated with the 100 vol % Ni layer placed in the die first. After each layer is added to the die, it is gently pressed to even out the layer. This pressing does not apply enough force to consolidate the powders, but is just enough to flatten the layer to allow for smooth interfaces. Once all of the powders have been inserted into the die, the ram is placed on top for pressing. The system is placed onto a

uniaxial press and compacted with a pressure of 86 MPa, based on prior thermal matching work [29].

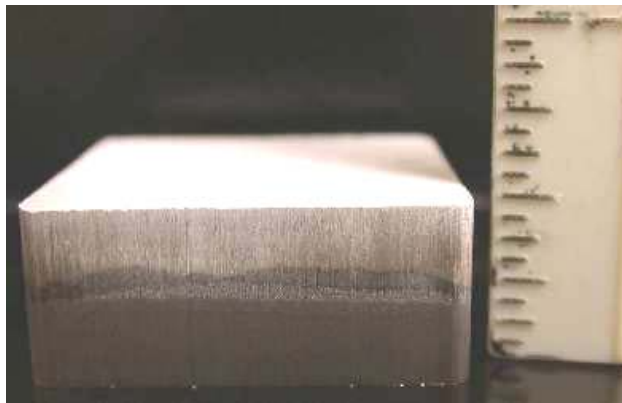


Figure 12. Green 12.7 mm FGM sample with 4 interlayers.

The green sample displayed in Figure 12 is then extracted from the die and is ready for sintering. The sample is placed into a tube furnace, shown in Figure 13 and is sintered under flowing argon following sintering cycle “A” shown in Figure 14.



Figure 13. Tube furnace used for sintering FGMs.

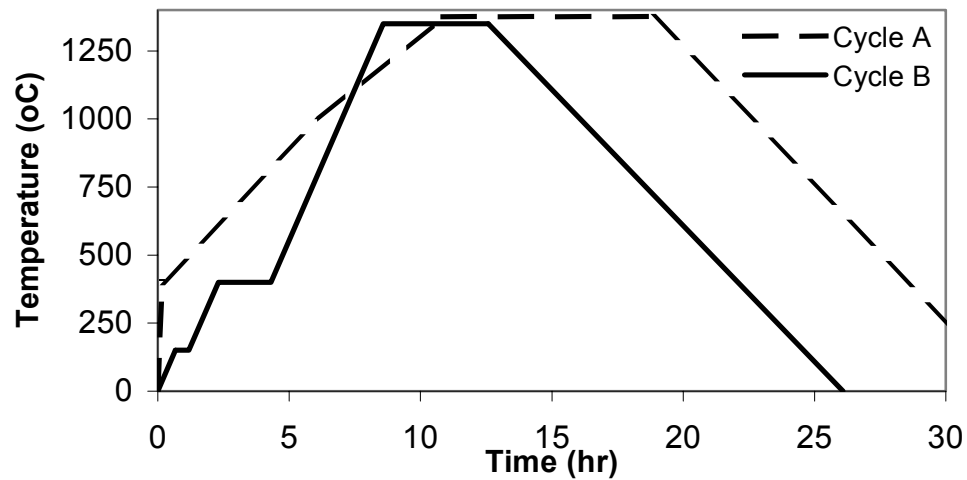


Figure 14. Two sintering cycles used for FGM fabrication.

The temperature was set at 1375°C due to the low melting temperature of nickel relative to alumina. The sample is sintered under flowing argon to prevent oxidation of the nickel at high temperatures. Since the sintering occurs under atmospheric pressure, a vacuum is not necessary inside the furnace, but an inert gas heavy enough to push the air out of the furnace is still required. A different sintering cycle “B” that sinters at 1350°C became the standard cycle used for FGM fabrication since it allows a more controlled burnout of the binder. The different sintering cycles did not contribute to different cracks forming, so the sintering cycle could be changed. Since the burnout temperature of the binder used in the FGMs is 400°C, by including an initial step increase to 400°C in cycle “A”, all of the binder will burnout in a very short amount of time, overwhelming the outlet of the furnace and seeping out of the furnace. However, in cycle “B”, the binder gradually burns out over a lengthened period of time, allowing its removal by the flowing argon.

After removing the sample from the furnace, the significant cracking in the material was viewed. As seen in Figure 15, two different cracks are present in the sample

following sintering. The first crack that occurs is located in the center of the graded region, between the 40 vol % Ni and 60 vol % Ni layers. It is believed this crack formed sometime after binder burnout while the samples was a weak powder compact, and is due to differential shrinkage stresses that arise during sintering due to the mismatch in material properties and consolidation rates. Since the layers begin shrinking at different temperatures and they shrink at various rates, shrinkage stresses evolve along the interfaces at the corners of the free edges. The interfaces in any layered material are the weakest point, due to the difficulty in transmitting a load across it. However, during sintering, the interface is even more of a threat for failure, since the material is not yet consolidated and the fracture toughness is very low.



Figure 15. 12.7 mm FGM with 4 interlayers after sintering.

Analysis of the fracture surface in Figure 16 reveals a coarse surface. The rough layer indicates that along this interface, the layers began sintering, and were pulled apart as they consolidated at different rates. The second crack, located in the 0 vol % Ni layer near the interface with the 20 vol % Ni, is due to thermal residual stresses in the specimen during the cooling. These stresses have been studied in the literature [5,16,18,20] and evolve not as a result of differential sintering shrinkage, but instead due to differences in the thermal expansion coefficients of the composite layers. The differences in the thermal expansion coefficients are much smaller than the differences in the shrinkage

rates. This fracture surface has a much smoother appearance than that of the previous crack. The formation of this crack likely occurs after the material has consolidated, and it propagates through the fully dense material.



Figure 16. Fracture surfaces for shrinkage stress crack (left), and residual stress crack.

A 25.4 mm thick sample with an identical type of distribution was fabricated. In this sample, the graded region is 8 mm, and each interlayer is 2 mm thick. The rationale behind this sample is that the thicker layers can better dissipate the stresses that evolve during sintering. However, as seen in Figure 17, the 25.4 mm samples showed similar cracking to the 12.7 mm samples.

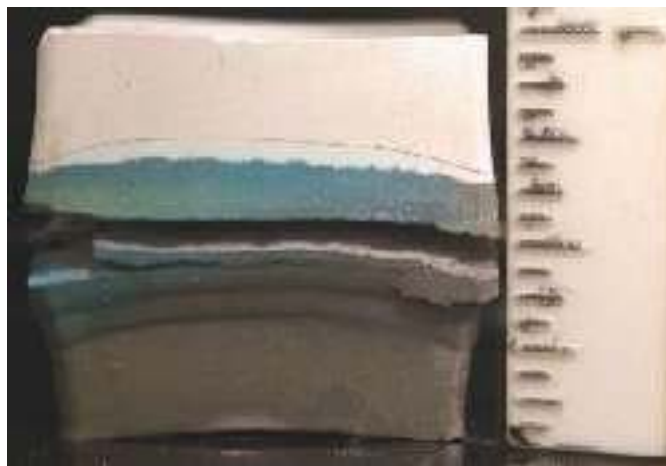


Figure 17. 25.4 mm FGM with 4 interlayers, after sintering.

Since the initial distribution failed at two different sample thicknesses, it was necessary to use a new distribution and incorporate thermal matching techniques as described earlier. The first method introduced to alleviate the stress evolution was the incorporation of a bimodal alumina distribution in the 0 vol % Ni layer, and a bimodal nickel distribution in the 100 vol % Ni layer, since these two layers exhibited the most shrinkage. The different bimodal distributions incorporated and their reductions in shrinkage are shown in Table 2.

Table 2. Reduction in layer thickness from different bimodal distributions.

vol % Ni	Alumina		Nickel		Shrinkage
	0.4 μm	18 μm	3 μm	17 μm	
0	100%				13.4%
0	75%	25%			5.7%
0	85%	15%			8.4%
100			100%		18.4%
100			50%	50%	16.2%
100			20%	80%	15.0%

Sintering the samples with the bimodal powder distributions continued to exhibit the types of cracks originally created, however, the severity of the deformation was much less than before. Instead of the layers on opposite sides of the delaminating crack pulling apart, they appear to have deformed in the same direction, as seen in Figure 18. While the alumina shrinkage was significantly reduced, the nickel seemed unaffected by the bimodal powder distribution. By adding the large particles, the shrinkage in the alumina layer was reduced enough to eliminate the deformation on the ceramic-matrix side of the FGM, but the addition of large nickel particles failed to reduce the deformation of the nickel-matrix regions of the FGM. The explanation for these differences lies in the materials themselves. In the alumina, the large particles remain rigid as the smaller

particles sinter around them. However, in the nickel layer, the large particles can deform during compaction, as well as during sintering as the smaller particles sinter.



Figure 18. 12.7 mm FGM with 4 interlayers and bimodal alumina layer.

Since the bimodal powder distribution did not lead to a crack-free sample, the distribution was altered to include two additional layers between the 0 vol % Ni and 20 vol % Ni layers: 5 vol % Ni and a 10 vol % Ni. Additionally, the sample was created with all eight layers having uniform thickness of 3.125 mm, instead of having uniform thickness for the interlayers with thicker pure layers. Moreover, the binder quantities were altered slightly to those in Table 3 to more closely match the green densities and sintering behavior of the layers.

Table 3. Adjusted binder quantities for all layers, including additional 5 and 10 vol % Ni layers.

vol % Ni	wt % Binder
0	3.5
5	3.9
10	4.1
20	3.5
40	3.5
60	1.1
80	0
100	0

After sintering the 25.4 mm sample, cracks were still found, but the locations had changed. The delaminating crack that was previously located near the 40 vol % Ni and 60 vol % Ni interface was located in the new samples near the 60 vol % Ni and 80 vol % Ni interface. Additionally, the cooling crack in the alumina layer was moved to the 10 vol % layer, as can be seen in Figure 19. The change in the location of the shrinkage crack is most likely due to the change in the gradient architecture to uniform layer thicknesses. When the cracks were located between the 40 vol % and 60 vol % Ni layers, the thickness of each base layer was the same as the thickness of the entire graded region. In 12.7 mm samples fabricated with uniform layer thickness, but without 5 vol % Ni and 10 vol % Ni layers, see Figure 20, the location of the delaminating crack was the same as the 25.4 mm thick sample with 5 vol % Ni and 10 vol % Ni included.

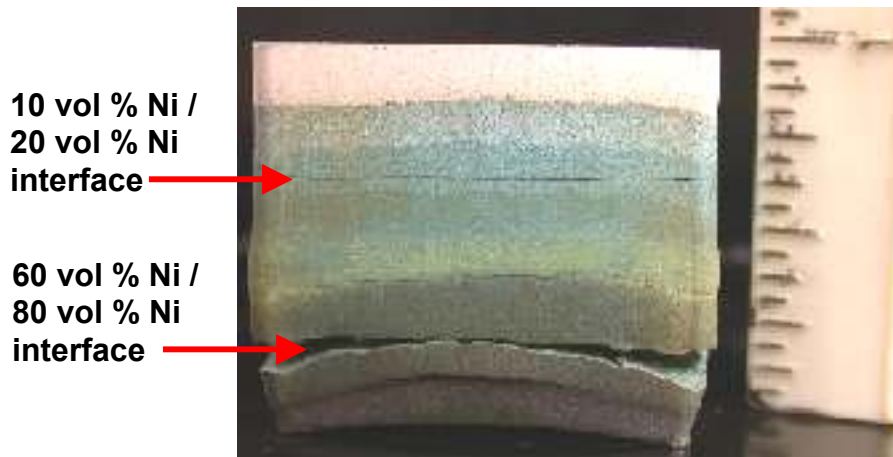


Figure 19. 25.4 mm FGM with 6 interlayers and uniform layer thickness.

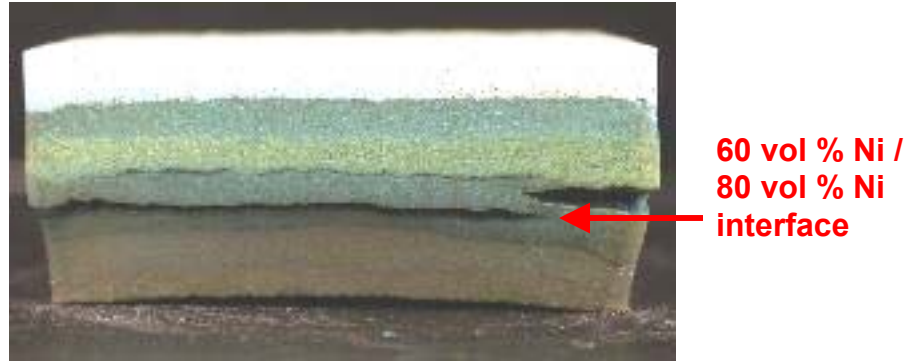


Figure 20. FGM with 6 total layers of uniform thickness, 12.7 mm thick sample.

It was postulated that the cracking might be a result of the large amounts of shrinkage in the pure base layers, causing them to pull the interlayers apart. In order to test the hypothesis that a crack would not form without these layers applying additional shrinkage stresses, a sample was fabricated consisting only of the six interlayers. The proposition was rebuffed when the large delamination crack seen in Figure 21 remained after sintering, indicating that the presence of the gradient architecture was primarily responsible.

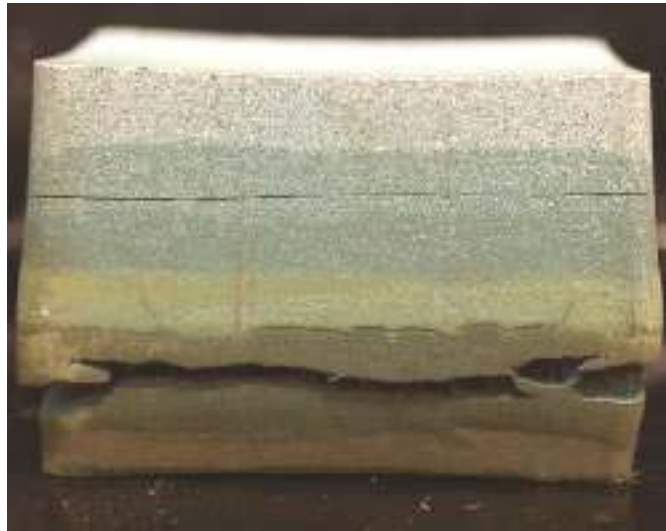


Figure 21. FGM consisting only of graded region no pure base materials, uniform 3.15 mm layers.

It may be necessary to alter the powder distributions within the interlayers in order to achieve the proper thermal matching of sintering behavior between layers; however, this would affect the microstructures and may adversely affect the mechanical properties of the FGM. To determine how much an effect the square cross-section was having on the formation of shrinkage cracks, specimens with circular cross-sectional geometries (i.e. axisymmetric cylinders) were also processed that did not possess the same stress concentrations present at the corners of the square cross-sections.

2.2.2 Circular Cross-Sectional Geometry

In addition to the square die that had been used to fabricate the graded specimens, a circular die with the dimensions shown in Figure 22 was used to fabricate FGMs with the distributions and powders previously used with the square die. Comparisons between the two geometries provided new insight into the importance of the geometrical effects on the shrinkage stresses of an FGM.



Figure 22. Die for circular specimens, with 1 in diameter.

Originally, the goal was to fabricate an FGM identical to the eight-layered 25.4 mm sample produced with the square die. The sample was created following the same

steps discussed earlier to fabricate the square specimen. After sintering, though, the final thickness of the sample was not 25.4 mm, as expected, but actually measured 38.1 mm. The discrepancy in the final dimensions of the circular sample is due, in part, to the fact that calculating the amount of powder necessary to make a sample of a desired thickness is a bit more challenging for a circular sample than it is with a square sample. The powder weight calculations for the square die were made for a given final thickness of a layer with a 25.4 mm x 25.4 mm cross-section, and they are reasonably accurate in producing the desired thickness. However, the final dimensions for the circular die did not scale accordingly, requiring the calculations to be slightly modified to properly predict the final size. Due to the improper calculations, the circular FGM cannot be directly compared to the previous square samples, because the circular sample tended more towards a rod than a plate. As a result of the rod-like geometry, stresses can be more easily dissipated, and the sample in Figure 23 was fabricated crack-free.



Figure 23. Crack-free circular specimen, roughly 38.1 mm, uniform layers.

Determination of the proper dimensions to use in the powder calculations allowed the creation of circular FGM samples 25.4 mm and 12.7 mm thick. While it was believed that circular samples would not develop the same thermal stresses during sintering as the square samples, due to the axisymmetric geometry and lack of stress concentrations at corners, the samples created with both the uniform thickness distribution and the thick base material distribution developed cracks. The results of these samples are shown in Figure 24.

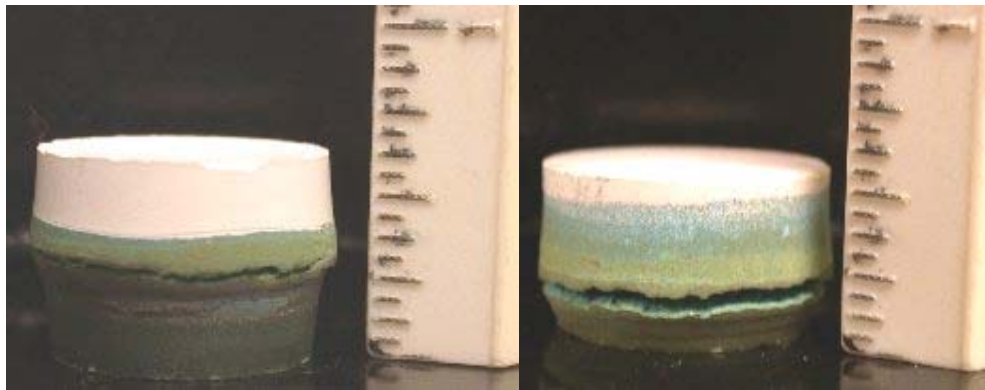


Figure 24. 12.7 mm FGMs with identical distributions to square samples; left has 4 interlayers, right has 6.

An important discovery was made when a crack-free 25.4 mm sample thought to have the standard eight uniform layer distribution was sintered. The sample, shown in Figure 25, has a radial bulge in the 40 vol % Ni and 60 vol % Ni layers, as well as in the 100 vol % Ni position, but it is not accompanied by any delamination or warpage in the axial direction.

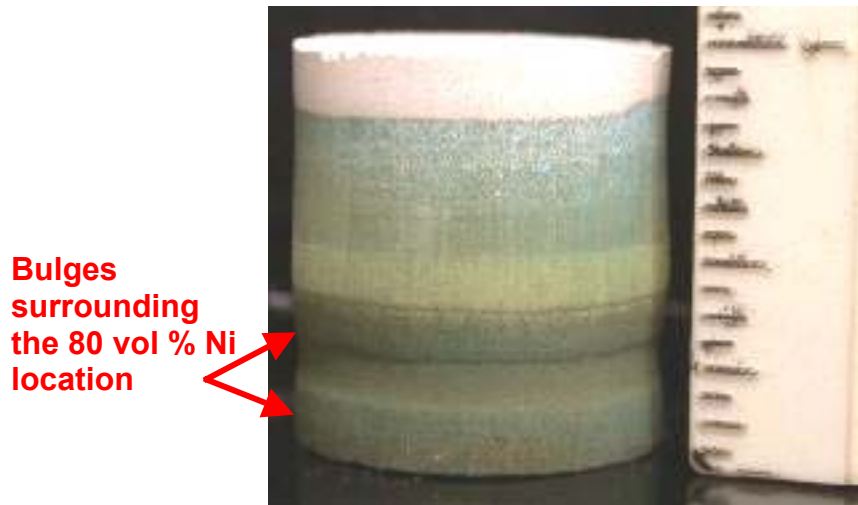


Figure 25. 25.4 mm FGM with no cracks, 8 layers with uniform thickness.

Additionally, 12.7 mm samples with identical distributions were also fabricated without any cracking present. However, observation of the microstructures of each layer revealed alumina particles in the 100 vol % Ni position. It was surmised that during preparation of different composite powder mixtures, some of the powders had been mixed up and improperly labeled, and that the layering was actually 0 vol % Ni, 5 vol % Ni, 10 vol % Ni, 20 vol % Ni, 40 vol % Ni, 60 vol % Ni, 100 vol % Ni, 80 vol % Ni.

However, when new powders were created, and a 12.7 sample was fabricated intentionally with the aforementioned distribution, a delaminating crack formed once again, as seen in Figure 26.

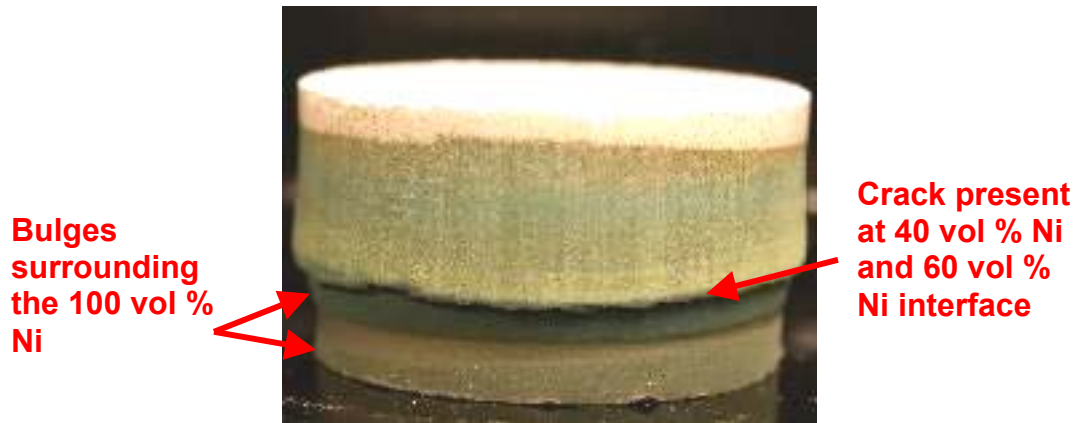


Figure 26. 12.7 mm FGM, with 100 vol % Ni and 80 vol % Ni layers inverted.

In addition, a symmetric FGM was fabricated with a thickness of 25.4 mm, basically consisting of two 12.7 mm FGMs with equally thick layers attached by their pure nickel layers. The rationale for this sample concerned the idea that the crack-free sample consisted of a 100 vol % Ni layer sandwiched between two layers that shrank much less than it, thus adding a constraint to its shrinkage. The symmetric distribution delaminated during sintering, seen in Figure 27, thus revealing that locating the pure nickel layer between two layers would not constrain its shrinkage enough to prevent the 80 vol % Ni region from pulling away from the 60 vol % Ni.

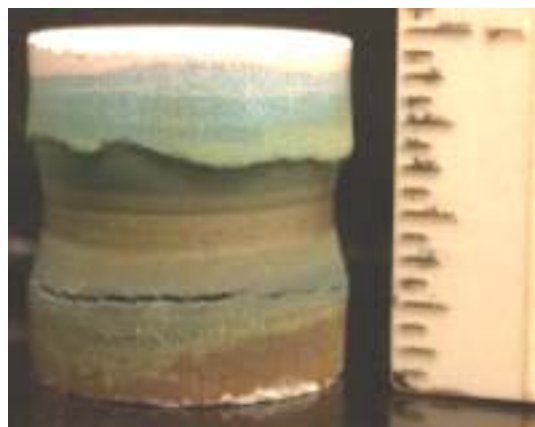


Figure 27. Symmetric FGM, equivalent to two 12.7 mm FGMs attached at the nickel layer.

In response to the previous results, an FGM was fabricated with all layers in their expected locations, except the pure nickel layer was replaced by a 60 vol % Ni layer. The cracking that occurred during sintering in the distribution with equal layer thickness is located between the two layers with the greatest difference in shrinkage, as shown in Table 4.

Table 4. Shrinkage data for each composite layer.

vol % Ni	Radial Shrinkage (%)	Shrinkage Difference (%)
0	8.12	
5	11.02	2.9
10	10.29	-0.73
20	9.22	-1.07
40	6.87	-2.35
60	6.91	0.04
80	14.57	7.66
100	18.22	3.65

As a result, the replacement of the pure nickel layer is intended to restrict the shrinkage of the 80 vol % Ni layer, even though these two layers exhibit the largest differential shrinkage. The sintering of this FGM distribution revealed no cracks, and exhibited the same bulging in the sample as initially observed. It also revealed that the cracking is due not only to the large differential shrinkage between the 60 vol % Ni and 80 vol % Ni layers, but it is also due to the fact that the pure nickel layer exacerbates the shrinkage of the 80 vol % Ni layer. By including a constraint on the 80 vol % Ni layer's shrinkage, reducing it roughly 20% from a radial shrinkage of 14.8% to 11.0%, the differential shrinkage between the layers can be reduced to a more manageable amount.

Chapter 3: Modeling the Sintering Behavior of Composites

Models for predicting the sintering behavior of the composites and evolution of shrinkage stresses in the graded specimens were developed based on the porosity in the FGM, in both the green and consolidated states. The calculations used in this model are useful in determining what characteristics of the gradient architecture are causing cracks to form, and may help in finding a solution to the problem. The calculations are based upon the volume fractions of nickel, alumina, and porosity present in each sample layer. The assumptions and calculations will be discussed throughout this chapter.

3.1 Porosity Model

3.1.1 Porosity Calculation

The first step towards characterizing the gradient architecture that is formed by pressureless sintering is to determine the porosity of the sintered composites. Calculations of porosity are made directly from measurements of density changes in the sintered composites. The samples used for these calculations are homogeneous disks, rather than graded materials, in order to determine accurate measurements of final mass, due to binder burnout, and accurate measurements of volume without the distortions attributed to gradients in shrinkage stress. The problems with determining the shrinkage data in this manner are: 1) the measurements can only be made after the sintering run is complete, not at the sintering temperature, which may introduce additional shrinkage, and 2) in the graded samples, shrinkage stresses may alter the shrinkage behavior from that observed in the homogeneous disks. It is anticipated that both of these effects will be negligible

given the rapid rate at which the disks are cooled and the level of stress that is experienced by the composites compared to that necessary to change sintering behavior. Each disk is fabricated based on the calculations for a 5 mm thick disk, as discussed in Chapter 2. Disks are fabricated for the following materials: unimodal 0 vol % Ni, bimodal 0 vol % Ni, 5 vol % Ni, 10 vol % Ni, 20 vol % Ni, 40 vol % Ni, 60 vol % Ni, 80 vol % Ni, and unimodal 100 vol % Ni. The disks were all pressed to roughly 86 MPa. The initial measurements of the diameter and thickness of each sample were taken prior to placing them into the furnace. The samples were all sintered in the furnace together up to 1350°C and held for four hours. Following removal from the furnace, the final diameter and thickness measurements were gathered, as well as the final mass. Using the measurements, the final density of the materials can be easily calculated. These values are shown in Table 5.

The initial density is determined based upon the final density and the amount of shrinkage, α , the composite has undergone. The shrinkage is typically measured in the radial direction, since that is the direction that causes the most damaging stresses in the graded material. The shrinkage stresses during sintering are a result of the differential shrinkage values in the radial direction, as discussed earlier. The shrinkage is used to back out the value of the initial green density of the materials, which can then be used to calculate the porosity. Assuming isotropy, a simple calculation, shown in equation (3-1), displays the change in the diameter as a proportion of the initial diameter. As can be seen in Table 4 in Chapter 2, the amount of shrinkage varies greatly from one material to the next.

$$\alpha = \frac{d_o - d_f}{d_o} \quad (3-1)$$

The shrinkage calculated from equation (3-1) is used to determine the changes in the volume of the specimen, which is then used to determine densities, ρ , and porosities, P . In order to determine the initial density, a mass balance is employed as follows:

$$\rho_o V_o = \rho_f V_f \quad (3-2)$$

The final volume can be rewritten as a function of the initial volume and the shrinkage assuming the changes in dimension are isotropic, which leads to the following:

$$V_f = V_o (1 - \alpha)^3 \quad (3-3)$$

After rearranging terms, the initial can be determined from the final density, which was determined previously, and the amount of shrinkage as follows:

$$\rho_o = \rho_f (1 - \alpha)^3 \quad (3-4)$$

The values of initial and final density computed from equation (3-4) can be seen in Table 5.

Table 5. Initial, final, and theoretical maximum density values for composites sintered to 1350°C.

vol % Ni	ρ_o (g/cm ³)	ρ_f (g/cm ³)	ρ_{th} (g/cm ³)
0 (unimodal)	2.32	3.40	3.94
0 (bimodal)	2.44	3.14	3.94
5	2.48	3.52	4.19
10	2.65	3.67	4.44
20	3.02	4.03	4.93
40	3.78	4.68	5.93
60	3.68	4.56	6.92
80	4.07	6.53	7.92
100	4.32	7.90	8.91

In order to calculate the porosity in the samples, the density values are compared to the Theoretical Maximum Density (TMD) for each composite layer based on a rule-of-

mixtures calculation. Equation (3-5) shows the calculation for the porosity, P , in the sample. The porosity values calculated from (3-5) are shown in Table 6.

$$P = \frac{\rho_{theoretical} - \rho}{\rho_{theoretical}} \quad (3-5)$$

Table 6. Initial and final porosities for composite layers sintered to 1350°C.

vol % Ni	P _i (%)	P _f (%)
0 (unimodal)	41	16
0 (bimodal)	38	20
5	41	16
10	40	17
20	39	18
40	36	21
60	47	34
80	49	18
100	52	11

3.1.2 First Theoretical Porosity Calculation

With the experimental values of the initial and final porosity in hand, it is necessary to determine if these values are consistent with a rule-of-mixtures prediction from the sintering behavior of each constituent phase (i.e., pure nickel powder and pure alumina powder), which can provide insight into what is happening during sintering. Therefore, each layer is considered to be a combination of nickel, alumina, and porosity, all of which are not only affected by the mixture of nickel and alumina, but also by the particle sizes of powder employed in the layer. In the current model, the theoretical porosity is assumed entirely due to the matrix material. That is, the particle reinforcement occupies a constant volume fraction of the layer before and after sintering, and all porosity is a result of the incomplete packing of the smaller particles of the matrix material, as shown in Figure 28. Therefore, these calculations are based upon the volume fraction of the matrix material present in a layer.

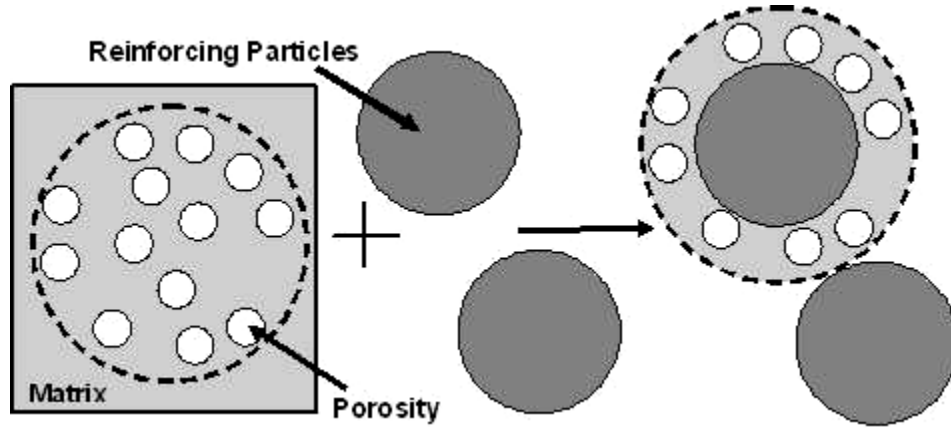


Figure 28. First theoretical porosity model, assuming all porosity is associated with the matrix.

The first step in this estimation is to determine the initial volume fraction of the matrix material prior to sintering. Using the initial porosity values, P_i , in Table 6, and the ideal volume fractions of nickel, v_{Ni} , the initial volume fraction of the matrix material, v_{matrix} , is determined by:

$$v_{matrix_i} = \frac{1 - P_i}{1 + v^*} \quad (3-6)$$

$$v^* = \begin{cases} \frac{1 - v_{Ni}}{v_{Ni}} & \text{for Ni matrix} \\ \frac{v_{Ni}}{1 - v_{Ni}} & \text{for Al}_2\text{O}_3 \text{ matrix} \end{cases} \quad (3-7)$$

The partial volume fraction, then, of the matrix with respect to the matrix and porosity is given by:

$$v_{partial_i} = \frac{v_{matrix_i}}{v_{matrix_i} + P_i} \quad (3-8)$$

Since all of the porosity is associated with the matrix material, the ratio of initial and final partial volume fractions should be equal to the ratio of initial, $(v_{pure})_i$, and final, $(v_{pure})_f$, volume fractions for the pure matrix material, as follows:

$$\frac{(v_{partial})_i}{(v_{partial})_f} = \frac{(v_{pure})_i}{(v_{pure})_f} \quad (3-9)$$

Now that the ratios of the matrix volume to particle volume and matrix material to porosity are known, the volume fraction of the matrix can be calculated. The calculation is based upon a summation of the volume fractions of each of the constituents:

$$v_{Ni} + v_{Al_2O_3} + v_{porosity} = 1 \quad (3-10)$$

Equation (3-10) can be rearranged in terms of the matrix and particle reinforcement:

$$v_{matrix_f} + v_{matrix_f} v^* + v_{matrix_f} \frac{1 - v_{partial_f}}{v_{partial_f}} = 1 \quad (3-11)$$

In (3-11), the ratio v^* defines the relationship between the two base materials and in the equation it converts the final volume fraction of the matrix into the volume fraction of the reinforcing particles. The third term on the left side of the equation is the conversion of the final matrix volume fraction to the volume fraction of porosity, and it employs the ration determined in (3-9). Equation (3-11) can be rearranged and solved for the volume fraction of the matrix, since all of the other values have been computed. The final porosity volume fraction is then calculated by subtracting the nickel and alumina volume fractions in equation (3-11), as follows:

$$P_f = 1 - v_{matrix_f} (1 + v^*) \quad (3-12)$$

3.1.3 Second Theoretical Porosity Calculation

In the previous model, the calculations were based upon determining the volume fraction of the matrix material and then backing out the volume fraction of porosity, assuming all porosity was associated with the matrix material itself, which is embodied in equation (3-9). Another model was created where the porosity associated with the matrix material was the same as for the pure matrix material, and all additional porosity was associated with the particles and could not be consumed during sintering, as shown in Figure 29. This model is initiated in the same way as the previous calculations, with equation (3-6). Instead of calculating the volume fractions through the matrix, though, the volume fractions are computed directly through the amount of porosity present.

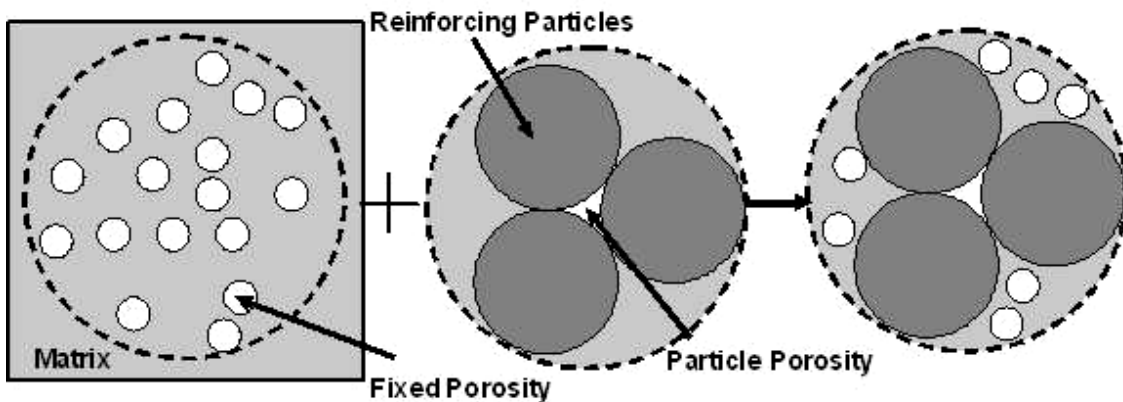


Figure 29. Second porosity model attributing an amount of porosity to the matrix equivalent to that of the pure material, and all remaining porosity associated with the particles.

With the value of the volume fraction of the matrix in hand, instead of calculating the partial volume fraction of the matrix material, the partial volume fraction of porosity attributed to the matrix is computed. This calculation is completed by scaling the volume fraction of the matrix based upon the amount of porosity associated with the pure matrix. Hence, the ratio of the initial porosity to the initial volume fraction of the pure matrix

material is used to convert the fraction of matrix material into the amount of porosity associated with the matrix. This conversion method assumes the matrix material behaves the same in each composite as it does when there is no reinforcing phase present. Therefore, the volume fraction of porosity associated with the matrix, $(v_{porosity})_{matrix}$, is given by:

$$\frac{(v_{porosity})_{matrix}}{v_{matrix}} = \frac{P_{pure}}{1 - P_{pure}} = constant \quad (3-13)$$

In (3-13), the amount of porosity due to the matrix material is computed using the known volume fraction of the matrix material, v_{matrix} , and the known ratio of porosity to matrix material. It is the embodiment of the key assumption in the second porosity model. The term P_{pure} is the amount of porosity in the pure matrix material. Following the calculation of the porosity in the matrix, the porosity associated with the presence of the reinforcing phase, $(v_{porosity})_{matrix}$, then, is simply the difference between the initial porosity in the material and the partial volume fraction of the porosity due to the matrix phase.

$$(v_{porosity})_{particle} = P_i - (v_{porosity})_{matrix} \quad (3-14)$$

The partial volume fractions of the matrix and reinforcing phases for each material are given Table 7, with the 0 vol % Ni values based on a bimodal mixture.

Table 7. Volume fraction of porosity due to the matrix phase and particle phases based on equation (3-14).

Vol % Ni	$(v_{porosity})_{matrix}$	$(v_{porosity})_{particle}$
0	0.41	0
5	0.39	0.02
10	0.37	0.03
20	0.34	0.05
40	0.27	0.09
60	0.34	0.13
80	0.44	0.05
100	0.52	0

Since the volume fraction of porosity is associated with the particles, it becomes a fixed third phase of the matrix and particle system. Therefore, its volume fraction relative to these two materials will always be the same. Thus, the volume fraction of porosity associated with particles in the sintered composite will have the following relationship to the volume fraction of the matrix:

$$\frac{((v_{porosity})_{particle})_{final}}{(v_{matrix})_{final}} = \frac{((v_{porosity})_{particle})_{initial}}{(v_{matrix})_{initial}} \quad (3-15)$$

A summation of all of the constituents, as in the first model, is the basis for determining the final volume fractions of the matrix and porosity. However, in this summation, the porosity is broken into two parts for the matrix and particle porosity:

$$v_{Ni} + v_{Al_2O_3} + (v_{porosity})_{particle} + (v_{porosity})_{matrix} = 1 \quad (3-16)$$

The equation in terms of the volume fraction of the matrix material is:

$$(v_{matrix})_f + (v_{matrix})_f v^* + (v_{matrix})_f \frac{((v_{porosity})_{particle})_{initial}}{(v_{matrix})_{initial}} + (v_{matrix})_f \left(\frac{P_{pure}}{1 - P_{pure}} \right) = 1 \quad (3-17)$$

Equation (3-17) can be solved for the final matrix volume fraction once the final porosity values are known. The final porosity, P_f , can then be determined from the porosity to material relationship shown in equation (3-13) using the final porosity from

the pure materials as P_{pure} and the relations for $(v_{porosity})_{matrix}$ and $(v_{porosity})_{particle}$ employed in equation (3-17), as follows:

$$P_f = (v_{matrix})_f \left[\left(\frac{P_{pure}}{1 - P_{pure}} \right) + \frac{((v_{porosity})_{particle})_{initial}}{(v_{matrix})_{initial}} \right] \quad (3-18)$$

3.1.4 Results

The experimental porosity measurements are shown in Figure 30, along with the results from both of the models described for the theoretical porosity. As can be seen in the plot, the theoretical estimates for the final porosity volume fraction are lower than what is observed during sintering. The differences between the estimated and measured porosities are larger in the nickel matrix regions, especially in the 60 vol % Ni layer. The two theoretical estimates follow similar trends, with the model allowing for particle porosity providing the lower of the two estimates.

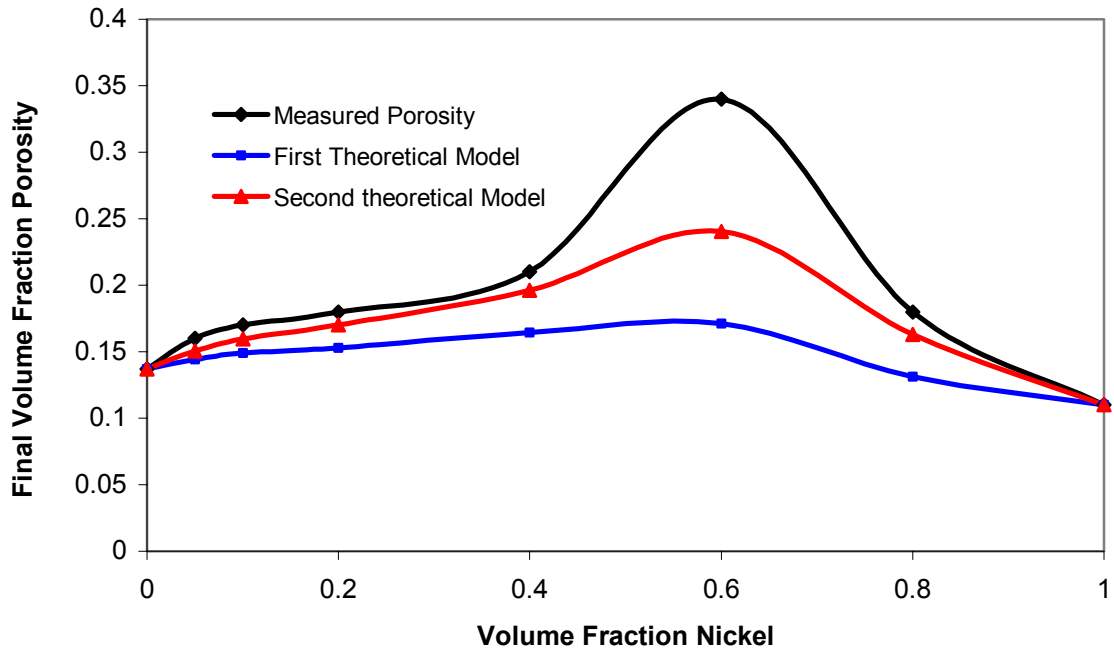


Figure 30. Plot of the measured and predicted values for the porosity, based on the two theoretical models.

An analysis of this plot sheds some light into a problem with the FGM fabrication. Specifically, the FGM layers are not sintering as much as they are expected to, with the nickel matrix regions displaying the largest discrepancies. During the fabrication of the FGMs, the cracking was attributed to poor matching of the sintering behavior of the layers. Now, the poor matching can be better explained, since it is seen that the porosity in the nickel-rich layers is not being consumed as much as it should. The lack of sintering in the alumina matrix layers, however, is not due to the lack of porosity consumption, but rather is due to the low sintering temperature used in the fabrication process. It is likely that a higher sintering temperature would enable the alumina region to sinter more fully, however, the nickel would be much nearer to its melting point. If the nickel melts, then the FGM will be unusable.

The poor sintering of the nickel, especially the 60 vol % Ni layer is possibly due to agglomerations within the alumina particles that prevent large areas of the nickel powder from consolidating. As discussed in Chapter 2, the agglomerations were slightly decreased by including ball mixing into the powder preparation. However, additional improvements in the mixing technique may be necessary to break apart the particle agglomerations, such as the inclusion of a dispersant or simply more rigorous mixing.

In Figure 31, the differences between the initial and final porosity is shown for the actual, as well as the theoretical porosities. The 60 vol % Ni layer can again be seen to exhibit the largest disparity between the actual and theoretical values. However, from this plot, it can be seen that if the 60 vol % Ni shrinkage were improved to agree more closely with the theoretical values, then it is likely that the 40 vol % Ni region would be the next layer that needs to be optimized. It is desired that the differential porosity curve be as smooth as possible, to allow a more gradual transition in shrinkage between the layers. Since the 40 vol % Ni layer would not experience as much porosity reduction, in the case of optimized 60 vol % Ni, its fracture toughness would probably not be high enough to prevent cracking in the FGM.

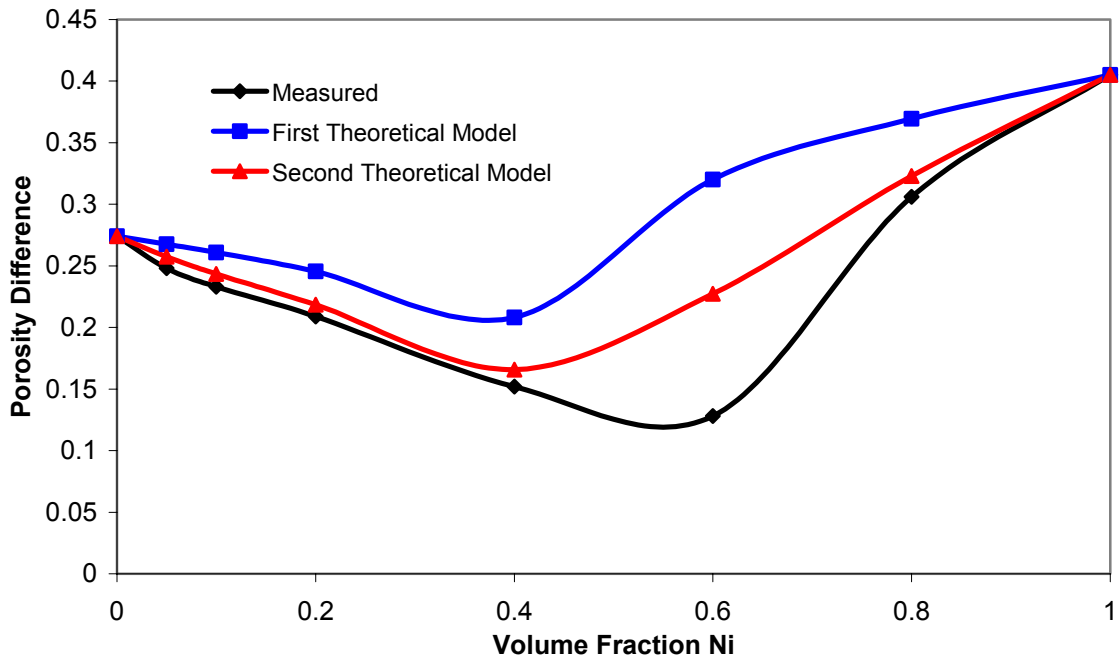


Figure 31. Plot of the calculated difference in porosity between initial and final values from the measured values and the two theoretical models.

The second porosity model provides a good estimation of the porosity measured in the composite layers, with the exception of the 60 vol % Ni layer. The close relationship between the predicted and measured values in the second model implies there is a contribution to the porosity of the specimen by the particles, possibly due to damage effects, and the overall porosity cannot be attributed solely to the matrix material. The problem associated with particle porosity is that it is not consumed during sintering and can lead to variations in the shrinkages of the layers of an FGM. The benefit of this porosity model is that it reveals the experimental porosity values are not completely unexpected, and it allows the focus to be directed onto a specific issue, rather than the larger issue of differential shrinkage stresses. Hence, in this case, particular attention

should be paid to the elimination of excess porosity in the 60 vol % Ni layer, which may be caused by ineffective compaction of the matrix in the green state.

3.2 Characterization and Modeling of Shrinkage

A model is desired to describe the shrinkage behavior of the composite layers during sintering. This model would allow for better predictions of the shrinkage of materials without necessarily sintering each composite. The shrinkage estimates can, in turn, be input into the finite element model to evaluate the stress evolution in a given material system.

3.2.1 Modeling of Shrinkage

In order to model the shrinkage of the layers in the eight-layered nickel-alumina functionally graded material fabricated in this research, the data had to be obtained. The best way to measure the shrinkage would be to sinter the composites and measure the deformation continuously. These types of measurements could be conducted using a dilatometer, and would additionally be made at the high temperatures. However, a dilatometer was unavailable for use in this research, and an alternative method had to be employed. In order to acquire the shrinkage measurements in this study, the composite layers were sintered to certain temperatures following sintering cycle “B” from Chapter 2. Once these points were reached, the samples were cooled following the same cooling rate as fully sintered samples would follow. The samples were measured once they reached ambient temperature. The drawbacks of this methodology are the additional deformation that may occur as a result of thermal contraction during cooling, as well as

additional consolidation that may occur during the initial stages of cooling from the higher temperatures. The thermal contraction is not as big of a factor at the low temperatures where there has been little consolidation of the composites, however, it may have a larger impact when cooling from higher temperatures as a result of a larger temperature difference than when sintering to lower temperatures. The shrinkage data acquired from these sintering experiments are shown in Figure 32.

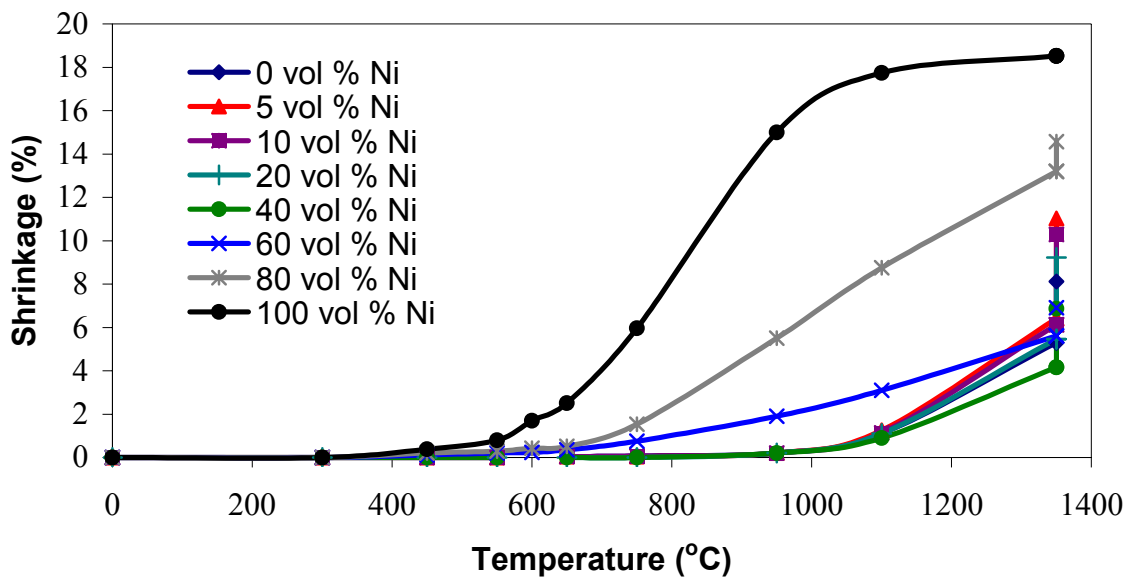


Figure 32. Shrinkage data from sintering experiments for each composite material in eight-layered graded material.

From the plot, it can be seen that the material mixtures with less than 60 vol % Ni exhibit similar sintering behavior until the temperature reaches roughly 1100°C, at which point their shrinkage behavior diverges. On the other hand, though, the behavior of the 60 vol % Ni, 80 vol % Ni, and 100 vol % Ni layers varies greatly from one layer to another.

The shrinkage differences between the layers with high nickel content leads to the large stresses that evolve during sintering, and consequently, failure through cracking

and debonding. It is necessary to be able to describe the nature of the shrinkage of these particular layers, since they lead to the FGM's failure. Beginning with the shrinkage data compiled through a number of sintering runs, an adequate fit is needed that incorporates the physics of the consolidation of the powders during sintering.

Sintering is a process that allows the boundaries of the powder particles to diffuse across one another to form a cohesive structure. Hence, a model must represent the fact that the shrinkage is the result of a diffusion-based process consisting of statistically random local shrinkage of the material with time at a given temperature. Therefore, a Weibull power law time-dependent exponential equation, consistent with the Kolmogorov-Johnson-Mehl-Avrami kinetic theory of nucleation and growth, was chosen as the basis for a model to fit the shrinkage strain [33]. The exponential model does provide some of the most important features in the shrinkage behavior. Specifically, when shrinkage begins in each layer, the materials initially exhibit sharp increases in the amount of shrinkage, due to the nucleation of loosely-packed particles at the outset of sintering. However, as sintering continues, the shrinkage levels off, due to the lack of small pores left to consume during growth, as well as the lack of energy to overcome the surface energy of the pore sizes that remain. The equations employed in the shrinkage model are as follows:

$$\varepsilon(t) = c_0 \left(1 - e^{-c_1 t^n} \right) \quad (3-19)$$

$$\frac{d\varepsilon}{dt} = c_0 c_1 n (t^{n-1}) e^{(-c_1 t^n)} \quad (3-20)$$

where the power law exponent, n , obeys a power law thermally-dependent exponential relationship as follows:

$$n(T) = c_2 \left(1 - e^{-c_3 T^p} \right) \quad (3-21)$$

In these equations, there are unknown coefficients c_0 , c_1 , c_2 , c_3 , and exponent p that are determined from fits to the shrinkage data shown in Figure 33.

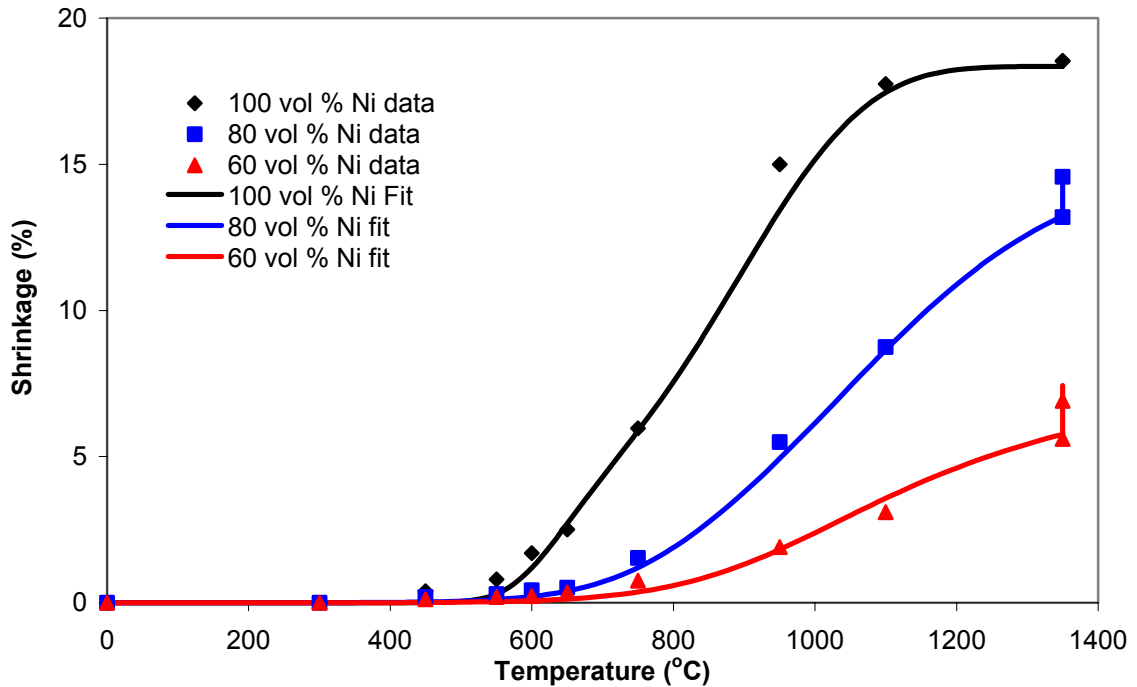


Figure 33. Measured shrinkage values for the three nickel matrix layers, along with the curves predicted by the shrinkage model.

This shrinkage model provides an adequate fit to the shrinkage data for the 100, 80, and 60 vol % Ni, as seen in Figure 33. The sintering behavior is initially flat for each composite, since the materials will not consolidate until they reach a temperature that provides enough energy into the system to initiate atomic diffusion. When the materials finally reach the maximum temperature, the model does a good job of predicting the total shrinkage that accumulates at that temperature. The values of the exponent, p , was 7 for

each case, and the coefficients varied as seen in Figure 34. It is clear that the introduction of the ceramic particles has a significant effect on the values of the coefficient, with only a slight change upon increasing the volume fraction.

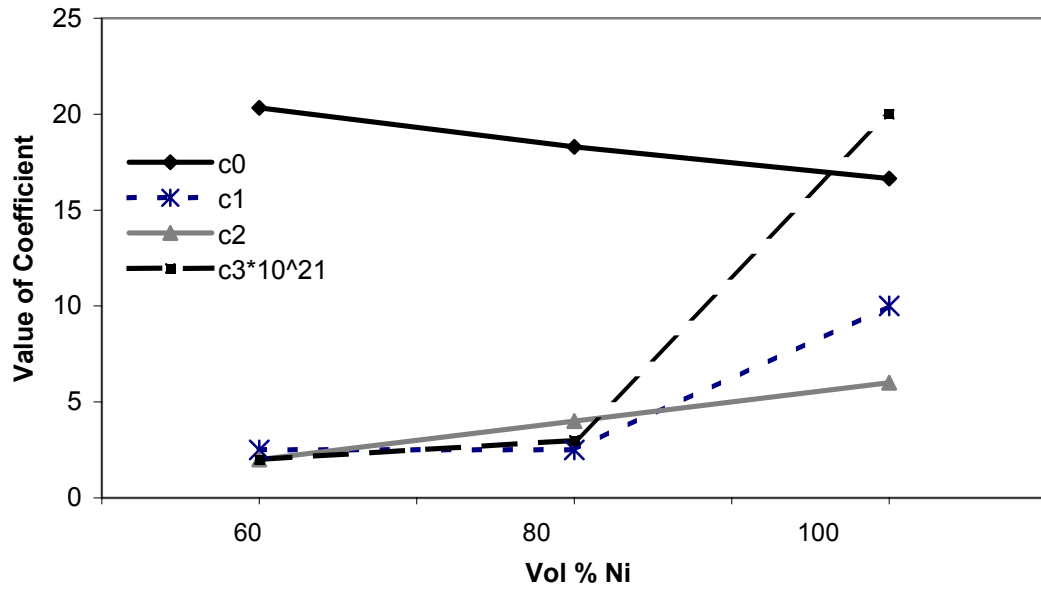


Figure 34. Value of coefficients for each volume fraction of nickel in the shrinkage model.

Chapter 4: Characterization of Gradient Architecture Evolution: Microstructure and Mechanical Properties

This chapter describes the characterization of the gradient architectures through the microstructures and mechanical properties of the pressurelessly sintered FGMs. Characterization is conducted on homogeneous specimens to baseline the evolution of the sintered composites, and then on the FGM specimens to characterize the gradient architecture.

4.1 Mechanical Properties: *Hardness Testing*

Mechanical properties can be determined quickly and easily using hardness testing, which is ideal for both sintered homogeneous composites and the FGM specimens. Hardness testing becomes more useful on the samples after sintering, since prior to densification (i.e., in a “green compact”), they are merely compacted powders held together by an organic binder with very small levels of stresses due to compaction. Hence, at this early stage in the process, the hardness test provides limited insight into the properties that can be expected from the fully sintered composites. While the hardness test used is a microhardness test, the size of the indentation was larger than the particulate reinforcement of the microstructure, allowing the FGM to be treated as a continuous media.

The hardness test used in this characterization is a Vickers microhardness test. The indenter is pyramid geometry with known angles on each side. Using a known load, the microhardness can be calculated by measuring the length of the diagonals of the indent on the surface of the material. Hardness is a measure of the localized plastic

deformation. Hence, ductile materials with elastoplastic deformation behavior will have a larger indent, while elastic materials, such as ceramics, elicit very little plastic deformation. Using equation (4-1), the load, p (in grams), and length of the indent's diagonal, l_{diag} (in millimeters), can be used to determine a value for the hardness.

$$HV = \frac{(1854 * p)}{\left(\frac{l_{diag}}{MF} * 1000\right)^2} \quad (4-1)$$

A microhardness test is used because it is a nondestructive test that can give an overall idea of the hardness of each layer based on constitutive assumptions. This type of hardness test, however, may lead to incorrect measurements if the tests are conducted in agglomerate regions. For instance, if there is a large alumina agglomeration in the 80 vol % Ni material, and the indenter is located completely within this region, the hardness value will likely read higher than the actual value for the material. An indentation that incorporates both matrix and reinforcing phases in a homogeneous composite would provide an optimal measurement, but it may violate constitutive assumptions on too large a scale. By minimizing the agglomerations, the errors in the microhardness measurements can be minimized.

While performing a hardness test of a green compact is of little or no value, conducting tests on a sintered structure more useful information can be gleaned into the degree of sintering (i.e., consolidation) and associated mechanical properties of the materials. For example, if the fully sintered material should have a microhardness of 1500 Vicker's, a typical value as shown in Table 8, then a value less than this would indicate that the material is only partially sintered with properties that are at some fraction of the fully sintered material. Since there can be significant variations in the

microhardness measurements, the relative consolidation and mechanical behavior is easier to ascertain when materials are harder. For nickel-alumina specimens, the nickel is very soft and has a hardness that tends to be an order of magnitude less than the alumina.

Table 8. Typical Vicker's hardness values for nickel and alumina [34].

	Typical Vicker's Hardness
Nickel	40
Alumina	1500

On the other hand, changes in the hardness of alumina with sintering will be much more significant. As a result, having an idea of the final hardness for alumina will provide an approximation to the amount of sintering the material has undergone. While there is not necessarily a direct relationship between these values, measuring hardness, for instance, an order of magnitude less than the expected value shows the sintering has only occurred to a limited degree. Using microhardness to characterize the degree of sintering will take on additional significance for the processing of FGMs due to the fact that alumina is a high temperature material, while nickel has a relatively low melting point in comparison. As a result, the ceiling for the sintering temperature is 1450°C, the melting point of nickel. However, alumina is best sintered at temperatures nearer to 1700°C. Therefore, it is difficult to reach maximum densification of the alumina in the FGM. Comparing the microhardness of the layers following sintering at different temperatures and after different durations held at the sintering temperature, the effect of different processing parameters, such as powder particle sizes and mixing techniques, on the degree of sintering and associated mechanical properties can be understood qualitatively. More importantly, the microhardness is a simple, non-destructive technique that can be easily used to characterize these effects along a graded interface.

The hardness values of disks sintered to 1350°C are shown in Figure 35. This data shows the hardness for each layer created from 0 vol % Ni to 100 vol % Ni, including unimodal and bimodal mixtures of the pure alumina.

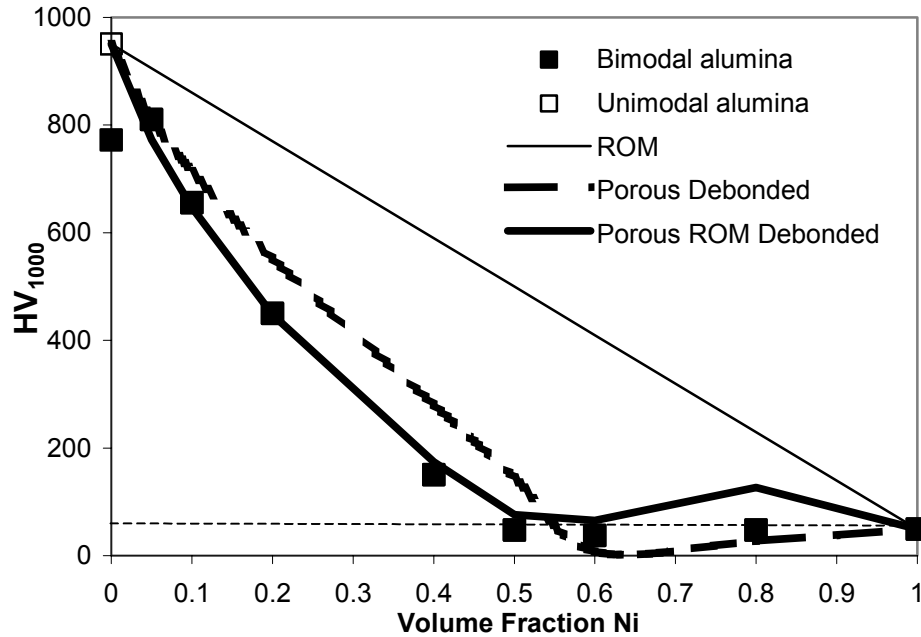


Figure 35. Vicker's microhardness values under 1000g load for each composite layer, including both unimodal and bimodal alumina for the 0 vol % Ni.

From the plots, the decreasing trend in the hardness can be seen accompanying the increase in nickel content through the ceramic-rich region of the material. This trend is expected, due to the increase in the ductile reinforcing phase. However, the bimodal alumina layer has a lower hardness than the 5 vol % Ni layer, most likely indicating that the large alumina particles had not sintered with the small alumina matrix. This is indeed verified by calculating the mechanical properties, p_{porous} for porous alumina given by the following relationship determined by Coble and Kingery [35]:

$$p_{porous} = p_{fully\ dense} (1 - 1.9 * P + 0.9 * P^2) \quad (4-2)$$

Assuming that the porosity for the bimodal alumina is equal to the volume fraction of large alumina particles, the value of Hardness would be 699. This is approximately 10% less than the value of 772.

The hardness values for the alumina matrix compositions, 5 vol % Ni to 40 vol. % Ni, can be compared with standard linear ROM predictions. The measurements are substantially lower than the ROM predictions. Once again, it appears that the nickel particles are not sintering with the alumina matrix. If the same analysis is used as for the bimodal alumina, the predictions are much closer to the measurements. However, they are almost identical to the measurements if the properties of the matrix are assumed to be the same as the ROM, but with the debonded particles acting as porosity. This is also true for the 50 vol % Ni specimen (which was fabricated for the purposes of characterization but not used in the gradient architecture), but the microstructure is an interpenetrating phase and not particle-reinforced. These effects are identical to those observed in elastic modulus measurements made on HIP (Hot Isostatic Pressed) composites by Bruck and Rabin [10].

Additionally, it is expected that the hardness would continue to decrease throughout the nickel region. However, the data reveals that the hardness measurements are nearly constant. Even though the Coble and Kingery model was developed for alumina, the same model is used heuristically for the metal matrix composites as well. The ROM porous prediction correlates well with the 60 vol % Ni specimen, however it is approximately $\frac{1}{2}$ of the prediction for the 80 vol % Ni. At that composition, the porous nickel prediction is more accurate. In the work of Bruck and Rabin, models were developed to describe the effects of the particle debonding on the elastoplastic behavior

of the composites, and could also provide more accurate predictions of the 80 vol % Ni hardness if necessary [10]. Regardless, all of the hardness measurements provide important insight into the need to treat the reinforcing phase as porosity in a ROM prediction of mechanical properties when developing processing and performance models of the graded metal-ceramic armor specimens.

4.2 Microstructural Characterization

In addition to measuring the hardness of the materials as discussed above, microstructural observations are also made to characterize the gradient architecture. These measurements are important to determine if the microstructure is particle reinforced or interpenetrating phase, which will not only impact the measured properties but the sintering behavior as well. The microstructural observations are made by placing the samples under an optical microscope and focusing on various regions of each layer. It is important to observe different locations within each layer, since the materials are not homogeneous on the microscale, and there may be features that are not present throughout the material.

When looking at the microstructure, the two base materials can be easily identified, and, thus, the observations can be used to make inferences into the behavior of the material during sintering, as well as some information regarding fabrication. Figure 36 shows the microstructures of the 0 vol % Ni through 100 vol % Ni materials after sintering. In each image, the darker material present is the alumina, while the lighter one is nickel. Each composite material layer has a distinct look that separates it from the other formulations. Specifically, depending on the volume fractions of each constituent

material, the final structure has a different appearance that can easily be compared to the neighboring layers. These observations are used to determine if the desired microstructure has been fabricated. For instance, in the 80 vol % Ni layer, a nickel matrix reinforced with alumina particles is preferred over a system of interpenetrating phases of the two materials for the desired mechanical behavior. As a result, the microstructure should appear as mainly light colored material with randomly located inclusions. The observations are utilized to determine whether or not the actual structure meets the desired specifications.

The two pure materials do not reveal much information, since the observations are not made at very high magnifications. In the microstructural images of all of the composites, the only phenomenon detected is the different phases present in each layer. The microstructural observations are not made on the sub-micron level, so features that are present in the pure materials at a smaller scale go unnoticed.

In the 5 vol % Ni and 10 vol % Ni materials, the microstructure is dominated by the ceramic matrix. The nickel particles are dispersed throughout the matrix. However, there are some regions with larger concentrations of nickel particles present in these layers. These agglomerations are indications that the composites are not homogeneously distributed, as desired. Additionally, these agglomerations may be one of the factors affecting the shrinkage, and therefore, the differential shrinkage stress distribution.

As the nickel content increases, in the 20 vol % Ni and 40 vol % Ni layers, the nickel regions begin to link together to create more of an interpenetrating matrix microstructure. As with the microstructures in the previous layers with lower metal contents, the particles form agglomerations rather than a fully dispersed structure.

The 50 vol % Ni composite is fabricated from “small” particle sized base materials. However, the nickel powder is an order of magnitude larger than the small alumina powder. This difference in particle sizes may help explain the microstructure found in this layer. A fully interpenetrating network was predicted for this particular composite, based on the microstructures observed in the 40 vol % Ni and 60 vol % Ni layers, along with the small particle size mixture of materials. While the structure nears that of a fully interpenetrating system, it largely appears to be that of a nickel matrix with alumina agglomerations.

In the nickel-matrix layers, the particle agglomerations become even more prevalent as the particle distribution shifts to small nickel and large alumina particle sizes. The 60 vol % Ni microstructure looks very similar to the 50 vol % Ni structure, although the two were fabricated with different particle sizes of alumina powder. Again, these agglomerations may be the cause of the poor sintering observed in the 60 vol % Ni layer.

The microstructural observations were useful during fabrication when, as mentioned in Chapter 2, a FGM was created crack-free with what was thought to be a standard distribution between 0 vol % Ni and 100 vol % Ni. However, the microstructure revealed particles present in the end layer that are not present in a pure nickel layer. These observations coupled with hardness testing revealed the layer was actually 60 vol % Ni.

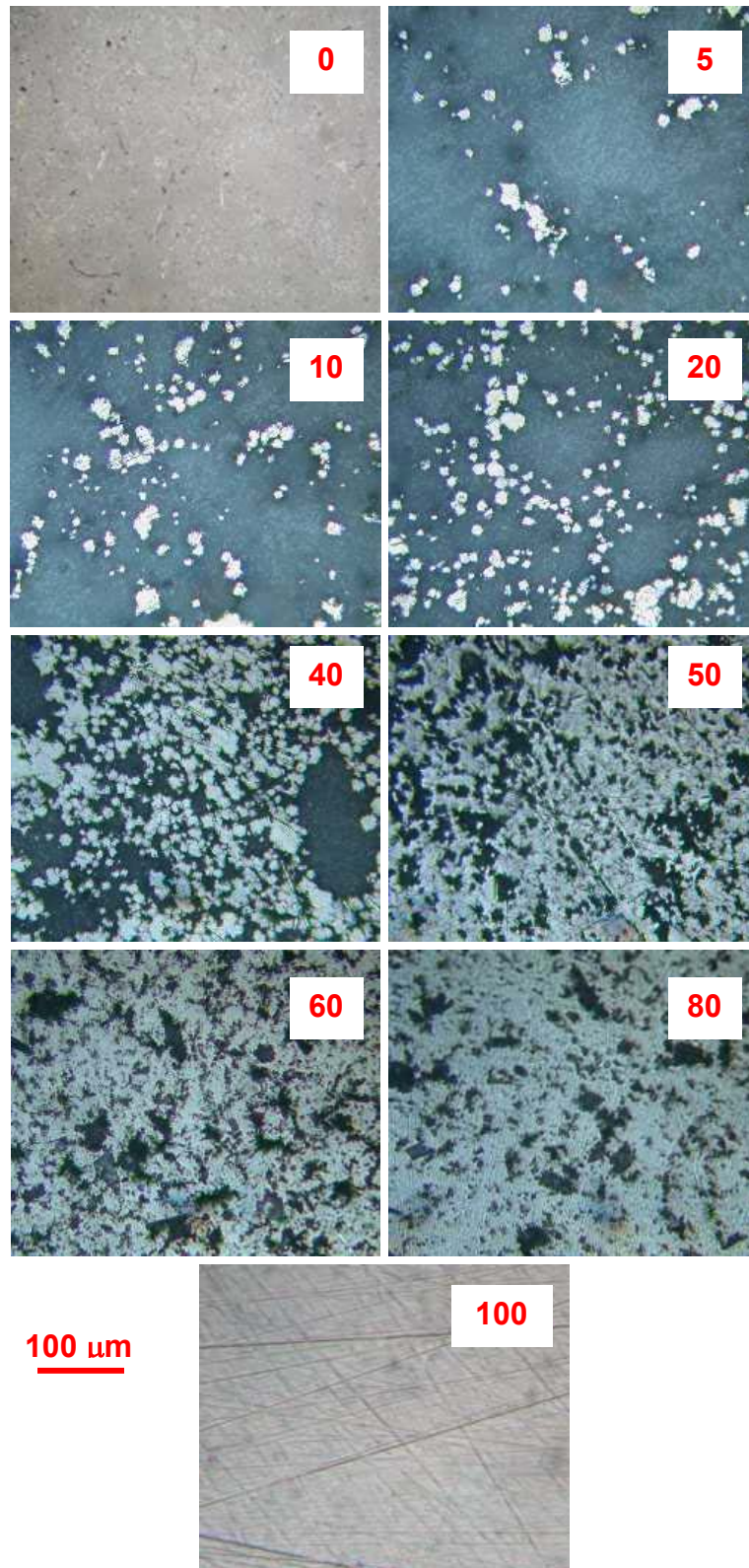


Figure 36. Microstructures for each composite material fabricated, labeled by percentage of nickel in the composite.

The microstructural observations are important in terms of the functional design of the FGM as well as for aiding in determining shrinkage problems. Since these FGMs are designed for armor systems, particle-reinforced microstructures are more favorable than interpenetrating phases. The observations can be used along with adjustments in particle sizes to determine whether or not the desired structure is being created.

Comparing the microstructures observed in Figure 36 with HIP microstructures fabricated in previous work shown in Figure 37 [10] reveals some of the problems with the current processing. The microstructures in Figure 37 illustrate well-dispersed reinforcement phases in the matrix materials. This dispersion can be contrasted with the current structures, which contain larger agglomerations and more interpenetrating phase structures than those from Bruck and Rabin. These agglomerations may introduce porosity, as indicated in the porosity model in Chapter 3, as well as decrease the antiballistic performance, along with the interpenetrating phase structure, of the armor specimens.

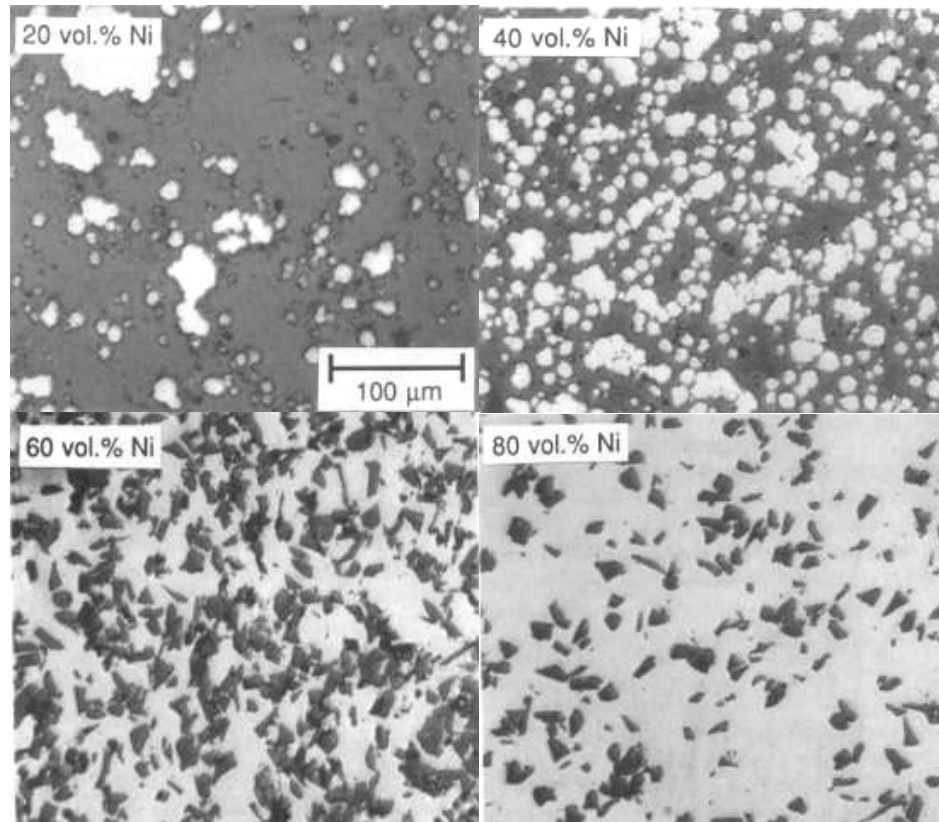


Figure 37. Microstructures from powder processed FGMs and consolidated by HIP [10].

Although the microstructures fabricated in this research are not ideal, and in fact may have a negative impact on shrinkage stresses, they are consistent enough with the microstructural assumptions made for the mechanical properties in the finite element analysis to be discussed in Chapter 5.

Chapter 5: Validation of Finite Element Model of Shrinkage Stress Evolution in Graded Specimens

In a related study, a finite element model has been developed, to describe the sintering behavior of the FGMs [36]. The importance of this modeling effort is in the important information it can reveal concerning the stress evolution in the material during the sintering process. In this thesis, the accuracy of the model is assessed by providing experimental measurements. The relative impact of the previously discussed porosity and shrinkage models can be tested using this model, to determine their effect on the shrinkage stress evolution.

5.1 Contributions of Porosity to Sintering Model

To develop the finite element model for the differential shrinkage stress evolution, a thermoelastoplastic constitutive equation for a particle-reinforced composite that accounts for the effects of micromechanical thermal stresses was used as the basis for describing the composite behavior [37,38]. Since shrinkage is introduced during sintering, its effects on the total strain had to be included in the original constitutive equations. The model assumes that the composite is macroscopically isotropic, consisting of brittle ceramic and ductile metal particles that are interspersed to fabricate the functionally graded material. In the composite system, the model assumes elastoplastic deformation in the metal particles and elastic deformation in the ceramic particles. In order to utilize the results from this thesis, porosity is included in the model by representing the void volume fraction, with the change in porosity being directly related to the shrinkage. [36].

Current porosity, in incremental analysis, is defined as the difference between the powder density and the current density of the specimen divided by the powder density.

Equation (3-5) can be rewritten as:

$$P = \frac{\frac{m}{V_{pd}} - \frac{m}{V}}{\frac{m}{V_{pd}}} \quad (5-1)$$

where m is the mass of the powder and V_{pd} and V are the powder volume and the current volume of the specimen, respectively.

Rearranging Equation (5-1) yields:

$$P = 1 - \frac{V_{pd}}{V} \quad (5-2)$$

Using equation (3-3) to represent the current volume of the specimen as a function of the shrinkage (which varies with the temperature, volume fraction of nickel, and powder particle size [29,39]) and the material's old volume, (5-2) can be rearranged to yield:

$$V_{pd} = (1 - P_o)V_o \quad (5-3)$$

Equations (3-3) and (5-3) can be substituted back into (5-2) to provide an expression for the current porosity of the material in terms of the original porosity and shrinkage.

$$P = \frac{(1 - \alpha)^3 - (1 - P_o)}{(1 - \alpha)^3} \quad (5-4)$$

The finite element model is based upon a functionally graded plate (FGP) with thickness, h , and width, d , [36]. The functionally graded plate simulates an actual functionally graded material during sintering. In order to model a sample similar to those

fabricated, the first FGP consisted of eight layers with different volume fractions to simulate the actual graded material. The volume fraction of alumina varied through the thickness direction from 0 vol % on the bottom layer to 100 vol % on the top. The initial alumina volume fractions of each layer are: 1, 0.95, 0.9, 0.8, 0.6, 0.4, 0.2 and 0, going from top to bottom. Samples with different geometries are also analyzed. First, blocks with square cross section $31.75 \times 31.75 \text{ mm}^2$ and thickness of 13.95 mm; second, cylinders with diameter 25.4 mm.

The functionally graded plate is assumed to deform according to the plane strain condition. The metal deformation assumes elastoplastic behavior governed by a von Mises yield condition, as well as isotropic hardening during consolidation. The ceramic material is assumed elastic. An 8-node-isoparametric element is used in the finite element analysis, with smaller elements near the interfaces. The temperature-dependent material properties are assigned at each node of the element and are interpolated according to a quadratic shape function within the element. The sintering process applied follows the heating cycle mentioned in Chapter 2 that heats to 1350°C and then cools.

The finite element model is based upon the assumption of macroscopically isotropic composite layers, in order to simplify the calculations. Additionally, this assumption allows for the use of the radial shrinkage value for the calculations, and not including the additional axial shrinkage. The axial shrinkage can differ from the radial measurement by as much as 20%, but that discrepancy may be due to a number of factors, such as a pressure gradient through the thickness direction during uniaxial pressing that creates a non-uniform green density within each layer. It is difficult to quantify the effect of such factors as the pressure gradient on the actual axial

deformation. Additionally, much of the previous modeling work applied to functionally graded materials has focused on isotropic behavior, allowing for the results of this work to be compared and validated against the previous models.

The model requires the input of certain variables in order to accurately calculate the stress evolution in a particular FGM. Specifically, the dimensions of the layers and their associated properties must be input into the model. Since the properties are changing with temperature, a relationship must be provided to describe their evolution. This relationship must be input into the model because the actual values of the properties are unknown as the material consolidates from a powder compact into a solid structure. Having the values of the properties at each temperature is unnecessary, however, because a relationship exists between the porosity in the composites and the properties themselves [34]. The porosity can be calculated by equation (3-5) based upon the shrinkage measurements shown in Figure 32.

5.2 Validation of Sintering Model

Before focusing upon the results of the stress evolution, the model must be verified against the experimental results in some manner in order to determine whether or not it is producing expected results. The best way to verify these modeling results is with the shape profile the model determines as a result of sintering. The model produces both stress and shape profiles, but it is very difficult to measure the stress evolution, whereas the shape profiles can be easily compared to one another.

5.2.1 Determination of Material Properties During Sintering

In order to progress with the model for this case, though, the material properties for all of the layers must be determined. It is difficult to measure the properties of the materials directly, because the materials begin as a powder compact prior to sintering into a dense material. Due to the non-linear nature of the property evolution during sintering, a simple interpolation of known values of the properties at different temperatures is not used. The change in the properties at different temperatures during sintering is not simply due to the thermal properties, but is also a result of the evolution of the composites themselves. Thus, a different method for calculating the material properties as the temperature changes must be applied.

As shown in Figure 32, as the temperature increases, the shrinkage increases, and the porosity decreases with a known relationship between the shrinkage and porosity. Since the shrinkage values are known based on the temperature, the porosity can also be calculated by equation (5-4). The shrinkage measurements are converted into equivalent porosity values in order to calculate the material properties. A relationship exists between the material properties and the amount of porosity in the material. The power law relationships shown in equations (5-26) and (5-27) between the Young's modulus and yield strength and fractional density is used to determine the properties based upon the porosity [34]. In these equations, σ_o and E_o are the fully dense properties, K is a constant related to the geometry and processing, V_S is the fractional density, and m and z are constants that depend on the density and pore structure, respectively. This relationship allows these material properties to be determined at each point during sintering based upon the evolution of porosity as follows:

$$\sigma = \sigma_o K V_S^m \quad (5-26)$$

$$E = E_o V_S^z \quad (5-27)$$

where:

$$V_S = \frac{P_{initial} - P_{current}}{P_{initial}} \quad (5-28)$$

5.2.2 Comparison of Theoretical and Experimental Shape Profile

Once the material properties can be calculated, the stress evolution and deformation of the FGM can be calculated by using the constitutive relations for any given inputs (i.e. initial geometry, distribution). The FGM profile following sintering can be output by the finite element model, and it can be compared to actual FGMs in order to validate the results of the model. It is easier to use the shape profile to validate the results than the stress profile, since the stresses are difficult to measure during the sintering process.

Figure 38 illustrates the profile view of an FGM and the results from the model for the final shape of that distribution, while Figure 39 shows the shape profiles from both images created with a digitizing software package. The distribution shown incorporates two 60 vol % Ni layers surrounding an 80 vol % Ni, as previously shown in Figure 25 from Chapter 2. This distribution yielded no cracking, but also has a unique shape with a dual bulge in the nickel-rich region of the FGM, rather than a single bulge in the middle of the composite.

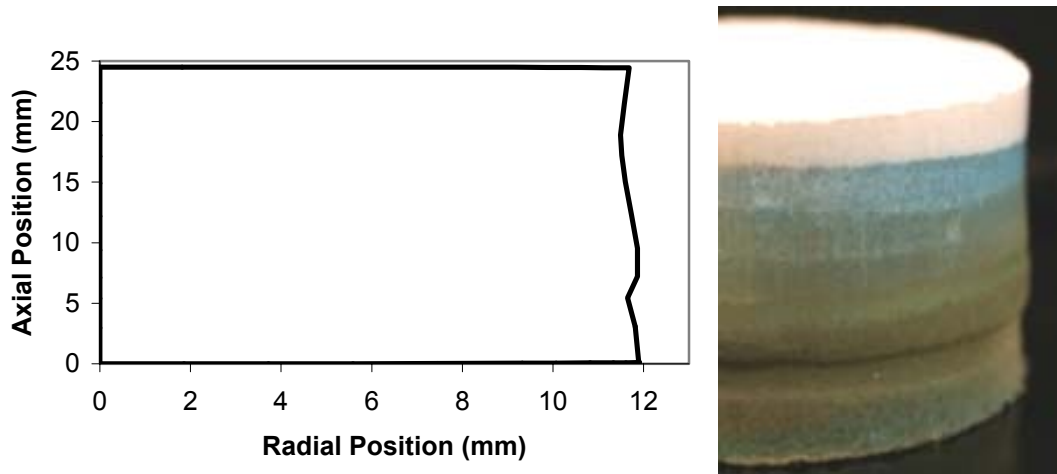


Figure 38. Shape profile for eight-layered FGM, with bottom three layers consisting of 60, 80, and 60 vol % Ni, from finite element model (left), and fabricated sample (right).

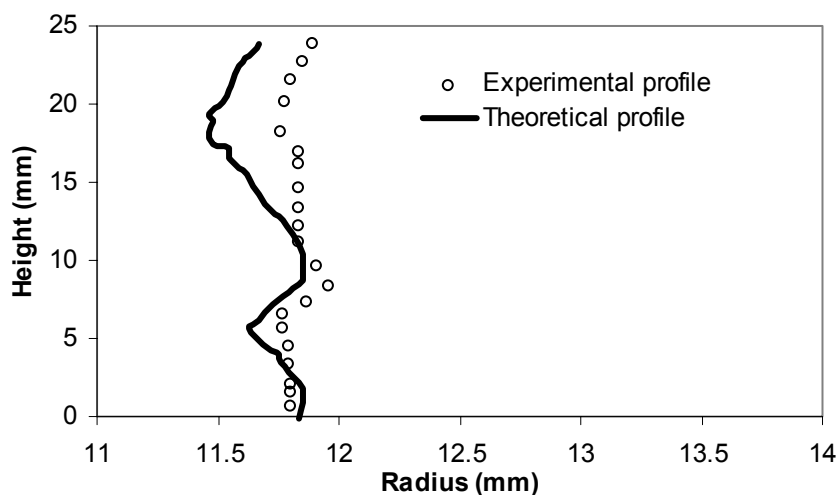


Figure 39. Outlines of shape profile for FGM sample and finite element analysis results, using digitizing software.

5.3 Stress Evolution During Sintering

In order to compute the stress profile, the model utilizes the assumption that there is no cracking in the FGM, which allows the stresses to reach values much higher than the critical values. It would be much more difficult to determine the stress profile without this assumption, due to various stress relief mechanisms, such as fracture, delamination, and plastic deformation.

The stress profile from the finite element analysis for the FGM illustrated in Figure 38 is shown in Figure 40. The stress profile shown below shows that the stresses in this sample do not reach the critical value, and hence, fracture is not predicted. As seen in Figure 38, this distribution with the 100 vol % Ni layer replaced by a 60 vol % Ni layer did not crack. It is believed that replacing the 100 vol % Ni with 60 vol % Ni adds a constraint to the shrinkage of the 80 vol % Ni layer, thus impeding its ability to fracture at the interface with the other 60 vol % Ni.

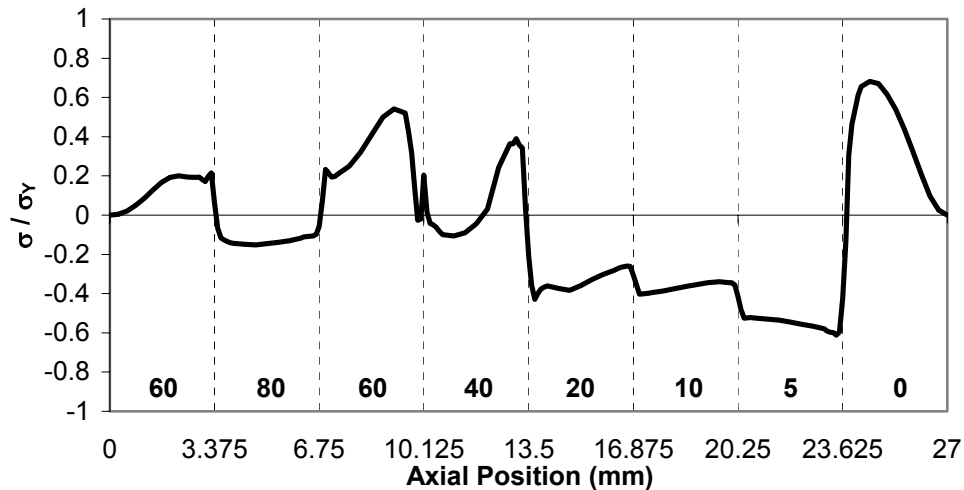


Figure 40. Stress distribution for 25.4 mm thick FGM with eight layers, and the 100 vol % Ni layer replaced by a 60 vol % Ni layer; % Ni content listed for each corresponding layer.

When the 80 and 100 vol % Ni layers are not included in the sample, the stress again does not reach a critical value, as shown in Figure 41. Since the crack typically forms between the 60 vol % and 80 vol % Ni layers, due to the large differential shrinkage between these layers, removing the 80 and 100 vol % Ni layers eliminates the largest differential shrinkage stresses from the FGM. As a result, as seen in Figure 42, this distribution does not fracture during sintering.

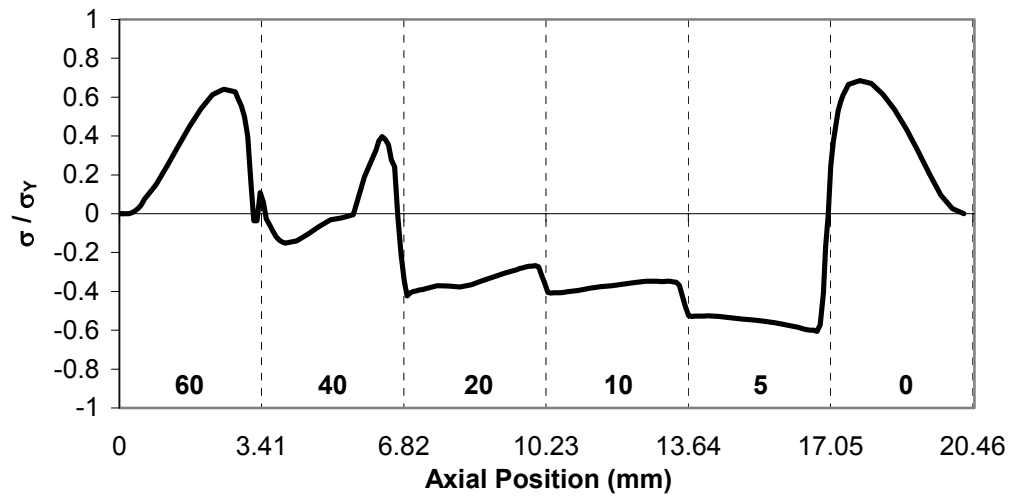


Figure 41. FGM without 80 vol % Ni and 100 vol % Ni layers%; Ni content listed for each corresponding layer.

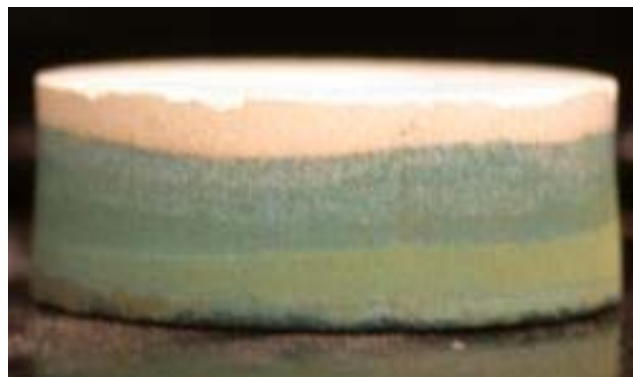


Figure 42. FGM fabricated without 80 vol % Ni and 100 vol % Ni layers, preventing fracture during sintering.

In addition to the circular geometries, the finite element model can also be used to calculate the stress profile in a square cross-section. As discussed in Chapter 2, no square samples were fabricated without fracturing, and this result is verified in Figure 43. The distribution reveals the stress reaches the critical value in the 60 vol % Ni layer, which is also where the cracks were located in the specimen, as shown in Figure 44. The distribution shown in Figure 43 was taken at 560°C, which is well before the maximum

temperature of 1350°C. Since the stress reaches the critical value at this temperature, the stress distributions produced at all ensuing temperatures cannot be validated, because the assumptions used in the analysis break down at this point. Specifically, the model does not allow for stress relief mechanisms that would take effect within the actual FGM following the initial fracture.

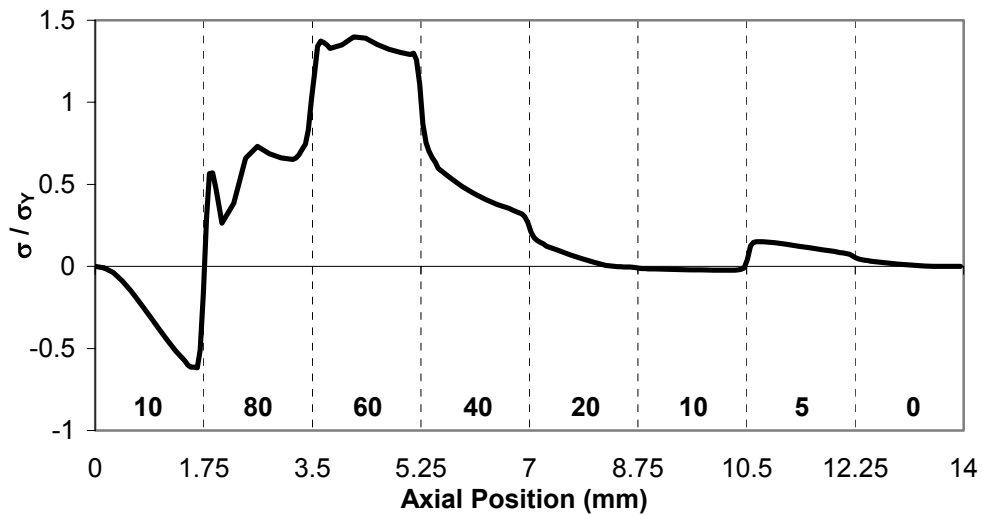


Figure 43. Stress Distribution at 560°C for 12.7 mm square geometry FGM with eight layers distributed with the labeled nickel volume content.

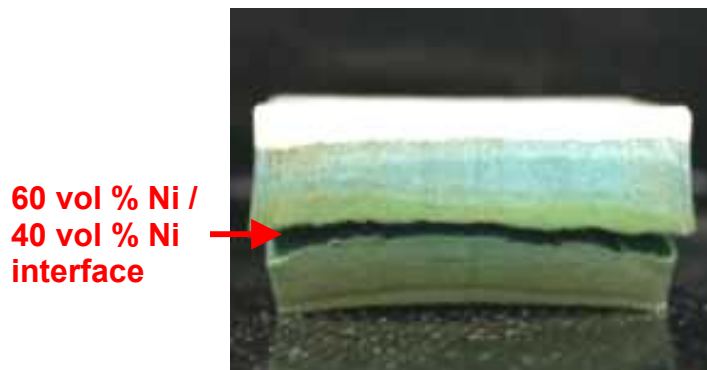


Figure 44. 12.7 mm square geometry FGM with eight layers following fabrication, with a crack in the 60 vol % layer near the interface with the 40 vol % Ni layer; the location of the maximum stress in the model.

The finite element model accurately predicts whether or not fracture is initiated in the FGMs fabricated in this study. The model can be used for multiple geometries in order to determine their suitability for fabrication. Any distribution can be modeled, as well as any geometry. The ability of the finite element model to predict fracture will allow the stresses of various modular geometries to be calculated in order to determine which one is most suitable for fabrication in an armor package. However, due to the assumption of no cracking utilized in the development of the model, the stress distributions can only be validated up to the temperature at which stresses reach critical values. Additionally, due to the difficulty of measuring the actual material property evolution, the specific shape of the distribution may have errors associated with it, but the location of the maximum values has been shown to provide accurate results.

Chapter 6: Conclusions and Future Work

The research presented in this thesis has made the following significant contributions to the pressureless sintering of ceramic-metal FGMs:

1. Development of procedure for pressureless sintering of metal-ceramic FGM armor specimens from metal and ceramic powders
2. Characterization and modeling of the evolution of shrinkage and porosity for homogeneous composites in gradient architecture
3. Characterization of microstructure in pressurelessly sintered metal-ceramic FGMs to compare particle dispersion with HIP composites
4. Measurement of microhardness to determine that the reinforcing phase should be treated as porosity in an ROM prediction of mechanical properties for the composites in the gradient architecture for processing and performance models
5. Verification of new sintering model quantitatively through direct comparison of warpage measurements and predictions, and qualitatively by determining and manufacturing gradient architectures with shrinkage stresses that will not cause cracking during pressureless sintering

6.1 Pressureless Sintering of Metal-Ceramic FGMs

Crack-free nickel-alumina FGMs have been fabricated following powder processing techniques and using pressureless sintering. Beginning with base powders, the appropriate mixtures of small and large particle sizes are created based upon thermal behavior and desired microstructural features. The base powders are layered in a die and uniaxially pressed to create a powder compact with a specified geometry and gradient architecture. The compact is consolidated through pressureless sintering in a furnace under an inert atmosphere.

In order to prepare samples without fracturing during consolidation, different types of gradient architectures are applied, and various material combinations must be

used. The purpose of these additional distributions and interlayer mixtures is to alleviate the stress evolution during sintering. By matching sintering behavior between adjacent layers as nearly as possible, the stresses that develop can be minimized, or at least delayed, to the point where the fracture toughness of each layer can withstand them. Delaying the stresses to a level where they do not overcome the fracture toughness implies one of two factors: 1) lowering the sintering temperatures of the materials or 2) reducing the shrinkage stress evolution.

Different material combinations can be applied to the composites to lower the sintering temperatures. For instance, using smaller particle size powders can improve the sintering behavior, as well as by decreasing the content of the reinforcing phase present in the layers. A lower temperature at which sintering begins equates to an earlier beginning to the actual consolidation of the material. In order for the fracture toughness of the material to be improved, the material structure must densify beyond that of individual particles and into one of a reinforced matrix composite.

On the other hand, another method to alleviate the stress evolution is to reduce the differential shrinkage present between the layers. There are different ways to approach this technique, but they based upon the principle of matching the sintering behavior of neighboring layers in a manner such that no layer shrinks significantly more than an adjacent one. As a result of better sintering matches, the reduction in the magnitude of the differential shrinkage stresses prevents the stresses from overcoming the fracture toughness. Hence, cracking can be prevented without explicitly improving the material properties, such as strength, but instead by improving the behavior in relation to the other materials.

6.2 Shrinkage Model for Predicting the Evolution of Porosity during Sintering

The matching of shrinkage is difficult because there are many factors that influence the overall sintering properties of each composite mixture. One method involves altering the materials themselves, such as when attempting to lower the sintering temperature mentioned before. Additionally, controlling the properties of the green compacts alters the amount of shrinkage that occurs in each layer. In the green sample, factors such as the porosity have a significant impact on the amount of shrinkage in the graded material, because the initial porosity is the voids into which the particles will move during sintering. These voids will be consumed throughout the sintering cycle as the particles consolidate into a single, cohesive structure. The porosity is a result of the space remaining between particles in a compacted state, as well as voids remaining after the removal of the binder by burnout.

The porosity is treated in this research as one of the guiding factors of the shrinkage. The porosity model described in Chapter 3 illustrates the issues dealt with during sintering. Specifically, in the current work, the issue of differential shrinkage stresses evolving as a result of the incomplete consumption of porosity in some layers of the FGM. As the model revealed, the porosity associated with the matrix is consumed during sintering, while the porosity embodied in the reinforcing particles is not consumed. Therefore, a larger fraction of porosity associated with the reinforcement phase leads to a reduction in consolidation and an increase in shrinkage stress.

The rate at which the porosity is consumed is directly related to the rate at which shrinkage occurs. However, this rate changes throughout the sintering cycle, as a result

of the temperature changes, as well as the material evolution that accompanies the temperature increases.

In order to adequately predict the sintering behavior for the different materials, a model was needed to describe the rate as a function of temperature. Since sintering is a diffusion-based process, a Weibull power law time-dependent exponential equation, consistent with the Kolmogorov-Johnson-Mehl-Avrami kinetic theory of nucleation and growth, was chosen as the basis for a model to fit the shrinkage strain. As a result, the exponent, which describes the rate of sintering, changes with the temperature, as well as with the amount of time the material is held at a constant temperature.

Since one of the main differences between modeling powder compacts and sintered, porous materials is the evolution of material properties. This property evolution governs many of the phenomena during sintering, such as the development of each material's strength, which is directly related to crack initiation and growth. This evolution occurs and varies as the temperature increases, but when sintering temperatures are reached the material will consolidate if the temperature is held constant at that point. As a result, the composite layers exhibit increasing sintering rates as the duration of hold increases. Applying a time-dependent model to the exponent, in addition to the overall sintering behavior, expresses this relationship.

6.3 Characterization of Pressurelessly Sintered FGMs

The nickel-alumina FGMs were characterized after sintering through microstructural observations and microhardness measurements. The microstructural observations are useful for determining the validity of the particle-reinforced matrix

composite assumption in the finite element analysis. Additionally, these observations are used to determine the type of structure obtained in the layers of an FGM. In all FGMs, the applications of the composite determine the type of properties necessary. These properties are governed by the microstructures that are fabricated. Specifically, in an armor application, the reinforced matrix structure is necessary for optimal antiballistic properties.

Microhardness measurements were used as a means of determining the relationship between the microstructure and properties of the sintered composites. The measurements were compared to rule-of-mixtures microhardness approximations that were modified to account for the degree of porosity in the composites. Since the porosity is directly related to the degree of sintering in the composite, the microhardness values can also be used as a qualitative method of characterizing how much consolidation the material has undergone during sintering. Microhardness measurements are therefore a potentially quick, nondestructive method for in situ analysis of the degree of consolidation in the gradient architecture.

The microhardness measurements demonstrated the need to represent the reinforcing phase as porosity in the calculation of material properties, since the measured data nearly matches the predictions from the ROM model with particle debonding. With the particles debonded from the matrix, the load cannot be shared between phases, and the particles have the same effect as porosity on the performance of the composite.

6.4 Validation of Porosity Effects in Finite Element Sintering Model

Finite element modeling is important in studying the stress evolution in functionally graded materials, since the stresses during fabrication can lead to cracking that renders the composite incapable of meeting its functional requirements. In addition to modeling the stresses for simple geometrical designs, it is also important to be able to model the stresses that develop in more complex geometries that may be useful for certain applications, such as armor applications in this research. These additional geometries would be costly to fabricate, due to the need for additional die creation for each shape, without the knowledge of the geometry's ability to sinter without crack initiation.

Incorporating the previously determined porosity effects into a recently developed finite element sintering model demonstrated the ability to predict the maximum stress location in graded composites. These locations correlated to the crack formation in graded composite specimens. The model also correctly predicted which gradient architectures and specimen geometries would not produce cracks. In order to provide the best results, though, it is important to have a reasonably accurate prediction of the evolution of material properties with sintering. Changing the property evolution, even a slight amount, can cause vastly different results from the model. This variation demonstrates the significant impact the properties of partially sintered microstructures will have on the sintering behavior of the graded specimens.

To incorporate porosity effects into the sintering model, a power law relationship was assumed to exist between the porosity and a material's yield strength, as well as between the porosity and the modulus of elasticity. The shrinkage model developed in

this thesis was used to determine the volume fraction of porosity present in each composite layer at various temperatures during sintering. Once the properties have been determined by using the volume fraction of porosity in the power law description of material properties, the stress evolution can be modeled and compared to the strength estimates to determine whether or not failure will occur in a gradient architecture and specimen geometry of interest. Thus, reasonable gradient architectures and specimen geometries can be determined for fabrication and testing.

6.5 Recommendations for Future Work

The fabrication and modeling of functionally graded materials can be extended into further areas of study. Fabrication work needs to be extended into more complex geometries of the graded composites. With a focus on armor applications, which was the guiding factor in choosing the materials in this research, modular geometries should be studied. These geometries allow the plates to fit together, but may minimize the stress evolution similar to round geometries.

In order to more closely model the actual material response in the modeling effort, obtaining accurate material property information during sintering may be an important area to study. This work requires the different composites to be sintered to various temperatures with properties such as yield strength and modulus of elasticity then measured at each temperature. Measuring these properties can be done in a manner similar to the porosity and shrinkage measurements taken in the current work. However, conducting measurements in this manner has disadvantages similar to the temperature-dependent shrinkage measurements. Specifically, since the measurements are not taken

at higher temperatures, they are merely an estimation of what the properties are at those temperatures. Additionally, an accurate testing method must be devised in order to determine the material properties of powder compacts that are not yet fully consolidated.

The finite element modeling can be extended into three dimensions in order to include the actual effect of the distributions on the stresses due to shrinkage in multiple directions. Three-dimensional modeling of the sintering allows a more comprehensive understanding of the problems that arise during the sintering of a layered functionally graded composite, and can provide additional insight into how to better optimize the designs.

Beyond the fabrication work, actual impact testing of the graded materials must be completed to understand the propagation of stress waves through a layered, graded composite. This type of research will determine the actual suitability of graded materials to armor applications. This testing requires a projectile to be fired at the functionally graded samples at a certain velocity to generate a stress wave through the material. This stress wave can be studied in order to determine the effect of the graded structure, as well as layering effects, on the composite's ability to absorb and dissipate the impact energy.

Bibliography

- [1] Chin, E.S.C., “Army focused research team on functionally graded armor composites,” *Materials Science and Engineering A-Structural Materials Properties Microstructure And Processing*, **259**, 155-161 (1999).
- [2] Matchen, B., “Applications of Ceramics in Armor Products,” *Key Engineering Materials*, **122-124**, 333-342 (1996).
- [3] Bruck, H.A., “A one-dimensional model for designing functionally graded materials to manage stress waves,” *Int. J. of Solids and Structures*, **37**, 6383-6395 (2000).
- [4] Mortensen, A. and S. Suresh, “Functionally graded metals and metal-ceramic composites: Part 1 Processing,” *Int. Materials Reviews*, **40**, 239-265 (1995).
- [5] Rabin, B.H., R.L. Williamson, and S. Suresh, “Fundamentals of Residual Stresses in Joints Between Dissimilar Materials,” *MRS Bulletin*, **20**, 37-39 (1995).
- [6] Suresh, S. and A. Mortensen, “Functionally graded metals and metal-ceramic composites: Part 2 Thermomechanical behaviour,” *Int. Materials Reviews*, **42**, 85-116 (1997).
- [7] Voigt, W., *Lehrbuch der Kristallphysik*, B.G. Teubner, Stuttgart, Germany (1928); *through [6]*.
- [8] Ravichandran, K.S., “Thermal residual stresses in a Functionally Graded Material system,” *Materials Science and Engineering A-Structural Materials Properties Microstructure And Processing*, **201**, 269-276 (1995).

- [9] Bruck, H.A. and B.H. Rabin, "Evaluation of Rule-of-Mixtures Predictions of Thermal Expansion in Powder-Processed Ni-Al₂O₃ Composites," *J. of the American Ceramic Society*, **82**, 2927-2930 (1999).
- [10] Bruck, H.A., and B.H. Rabin, "Evaluating microstructural damage effects in rule-of-mixtures predictions of the mechanical properties of Ni-Al₂O₃ composites," *J. of Materials Science*, **34**, 2241-2251 (1999).
- [11] Meyers, M.A., *Dynamic Behavior of Materials*, John Wiley & Sons, Inc., New York (1994).
- [12] Berezovski, A., J. Engelbrecht, and G.A. Maugin, "Numerical simulation of two-dimensional wave propagation in functionally graded materials," *European J. of Mechanics A/Solids*, **22**, 257-265 (2003).
- [13] Han, X., G.R. Liu, and K.Y. Lam, "Transient waves in plates of functionally graded materials," *Int. J. for Numerical Methods in Engineering*, **52**, 851-865 (2001).
- [14] Wilkins, M.L., C.F. Cline, and C.A. Honodel, "Fourth Progress Report of Light Armor Program," Lawrence Radiation Laboratory, Livermore, CA, Report No. UCRL 50695 (1969); *through [2]*.
- [15] Markworth, A.J., K.S. Ramesh, and W.P. Parks Jr, "Review: Modelling studies applied to functionally graded materials," *J. of Materials Science*, **30**, 2183-2193 (1995).
- [16] Williamson, R.L., B.H. Rabin, and J.T. Drake, "Finite element analysis of thermal residual stresses at graded ceramic-metal interfaces. Part 1. Model description and geometrical effects," *J. of Applied Physics*, **74**, 1310-1320 (1993).

- [17] Kawasaki, A. and R. Watanabe, "Finite Element Analysis of Thermal Stresses of the Metal/Ceramic Multi-Layer Composites with Controlled Composition Gradients," *J. of the Japan Institute of Metals*, **51**, 525-529 (1987); *through [16]*.
- [18] Drake, J.T., R.L. Williamson, and B.H. Rabin, "Finite element analysis of thermal residual stresses at graded ceramic-metal interfaces. Part 2. Interface optimization for residual stress reduction," *J. of Applied Physics*, **74**, 1321-1326 (1993).
- [19] Rabin, B.H., R.L. Williamson, H.A. Bruck, X.L. Wang, T.R. Watkins, Y.Z. Feng, and D.R. Clarke, "Residual Strains in an Al₂O₃-Ni Joint Bonded with a Composite Interlayer: Experimental Measurements and FEM Analysis," *J. of the American Ceramic Society*, **81**, 1541-1549 (1998).
- [20] Bruck, H.A. and A.L. Gershon, "Three-dimensional effects near the interface in a functionally graded Ni-Al₂O₃ plate specimen," *Int. J. of Solids and Structures*, **39**, 547-557 (2002).
- [21] Gasik, M.M., "Micromechanical modeling of functionally graded materials," *Computational Materials Science*, **13**, 42-55 (1998).
- [22] Yin, H.M., L.Z. Sun, and G.H. Paulino, "Micromechanics-based elastic model for functionally graded materials with particle interactions," *Acta Materialia*, **52**, 3535-3543 (2004).
- [23] Williamson, R.L. and B.H. Rabin, "The effect of interlayer properties on residual stresses in ceramic-metal joining," *Proceedings of the American Ceramic Society, 1996 Annual Meeting*, Indianapolis, IN (1996); *through [3]*.

- [24] Rabin, B.H. and R.L. Williamson, "Design and Fabrication of Ceramic-Metal Materials," *Processing and Fabrication of Advanced Materials III, Materials Week '93*, Pittsburgh, PA (1993).
- [25] Watanabe, R., "Powder Processing of Functionally Gradient Materials," *MRS Bulletin*, **20**, 32-34 (1995).
- [26] Mizuno, Y., A. Kawasaki, and R. Watanabe, "Measurement of Nonuniform Sintering Shrinkage of Functionally Gradient Material by Digital Image Processing," *Metallurgical and Materials Transactions*, **26B**, 75-79 (1995).
- [27] Matsumura, S., C. Uyemura, M. Okada, I. Yoshikawa, M. Togawa, and Y. Kuroda, in *Functionally Gradient Materials*, San Francisco, CA, *Ceramic Transactions*, **34**, (ed. J.B. Holt et al.), 331-338, Westerville, OH, American Ceramic Society (1993); *through [4]*.
- [28] Rabin, B.H. and R.J. Heaps, "Powder Processing of Ni-Al₂O₃ FGM," *Ceramic Transactions*, **34**, 173-180 (1993).
- [29] Winter, A.N., B.A. Corff, I.E. Reimanis, and B.H. Rabin, "Fabrication of Graded Nickel-Alumina Composites with a Thermal-Behavior-Matching Process," *J. of the American Ceramic Society*, **83**, 2147-2154 (2000).
- [30] Zhang, B. and M.M. Gasik, "Stress evolution in graded materials during densification by sintering processes," *Computational Materials Science*, **25**, 264-271 (2002).
- [31] Shinagawa, K. and Y. Hirashima, "Viscoplastic Stress Analysis of Shrinkage and Warping in Graded Layers during Sintering," *Key Engineering Materials*, **233-236**, 785-790 (2003).

- [32] Gasik, M. and B. Zhang, "A constitutive model and FE simulation for the sintering process of powder compacts," *Computational Materials Science*, **18**, 93-101 (2000).
- [33] Porter, D.A. and K.E. Easter, "Phase Transformation in Metals and Alloys", 2nd Edition, Chapman & Hall, London (1992).
- [34] German, R.M., *Sintering Theory and Practice*, John Wiley & Sons, Inc., New York (1996).
- [35] Coble, R.L. and W.D. Kingery, "Effect of Porosity on Physical Properties of Sintered Alumina," *J. of the American Ceramic Society*, **39**, 377-385 (1956).
- [36] Private Communication with Shabana, Y.M., University of Maryland, College Park, MD (2004).
- [37] Asakawa, A., N. Noda, K. Tohgo, and T. Tsuji, "Constitutional Equations of Thermal Stresses of Particle-Reinforced Composite" *JSME Series A*, **60**, 1632-1637 (1994).
- [38] Noda, N., S. Nakai, T. Tsuji, "Thermal Stresses in Functionally Graded Material of Particle-Reinforced Composite" *JSME Series A*, **41**, 178-184 (1998).
- [39] Winter, A., "Synthesis of Ni-Al₂O₃ Composites with Graded Microstructures: Deformation Analysis with Phase Shifted Moire Interferometry," *Ph.D. Thesis*, Dept. of Metallurgical and Materials Engineering, Colorado School of Mines, Golden, CO (1999).